



Universiteit  
Leiden  
The Netherlands

## Designing a Novel eV-TEM Gun in COMSOL

Cheng, Zhiyuan

### Citation

Cheng, Z. (2022). *Designing a Novel eV-TEM Gun in COMSOL*.

Version: Not Applicable (or Unknown)

License: [License to inclusion and publication of a Bachelor or Master thesis in the Leiden University Student Repository](#)

Downloaded from: <https://hdl.handle.net/1887/3453471>

**Note:** To cite this publication please use the final published version (if applicable).



---

# Designing a novel eV-TEM gun in COMSOL

---

THESIS

submitted in partial fulfillment of the  
requirements for the degree of

MASTER OF SCIENCE

in

PHYSICS AND ASTRONOMY

Author : Zhiyuan Cheng  
Student ID : 2673568  
Supervisor : Prof. Dr. Ir. Sense Jan van der Molen  
Second corrector : Prof. Dr. Ir. Tjerk Oosterkamp

Leiden, The Netherlands, July 3, 2022



# Designing a novel eV-TEM gun in COMSOL

**Zhiyuan Cheng**

Huygens-Kamerlingh Onnes Laboratorium, Universiteit Leiden  
P.O. Box 9500, 2300 RA Leiden, The Netherlands

July 3, 2022

## **Abstract**

We designed a new eV-TEM gun by using a field emission electron tip. We determined the best collimation voltage to be around 520 V. This is valid for electrons with landing energies varying from 1 eV to 100 eV. The angle distribution of electrons is improved down to around  $1^\circ$ , which is much smaller than that in the previous design (around  $10^\circ$ ). We also simulated the lensing effect near the TEM-grid, which enables us to calibrate the current profile incident on the camera in ESCHER.



# Contents

<b>1</b>	<b>Introduction</b>	<b>1</b>
<b>2</b>	<b>Background</b>	<b>5</b>
2.1	Electrostatic Lens	5
2.2	Field Emission	8
2.3	Electron Microscopy	11
2.3.1	LEEM and eV-TEM	13
2.3.2	Mean Free Path	16
<b>3</b>	<b>eV-TEM Gun</b>	<b>21</b>
3.1	Methods	21
3.1.1	Geometry	21
3.1.2	Time Steps	23
3.1.3	Emission area	25
3.2	Results and Discussions	26
<b>4</b>	<b>Lensing Effect of the TEM-grid</b>	<b>37</b>
4.1	Methods	37
4.2	Results and Discussions	38
<b>5</b>	<b>Conclusion</b>	<b>47</b>
<b>6</b>	<b>Acknowledgement</b>	<b>49</b>



# Introduction

The emergence of Electron Microscopy (EM) has paved the way to study materials with higher spatial resolution than traditional optical microscopes. By studying the mean free path (MFP) of the electrons when transmitting in the samples, EM can be a powerful tool to “visualize” the internal structures and study transport properties of the materials of interest[1]. Over the past few decades, the advance of energy filtering, which enables high-spatial-resolution microscopy, and aberration correction optics has even allowed us to observe microscopic structures at atomic scales[2]. According to Rayleigh’s criterion, shorter wavelengths will provide higher spatial resolution, thus by using high-energy (keV or even MeV) electron beams, sub-Ångstrom resolution could be realized in EM[3, 4]. However, electrons at such high energy could easily break bonds between atoms and thus damage the samples, thus EM’s operating at kilo-electron volts or even higher energy would not be ideal to study materials that are radiation sensitive[5]. Studies on 2D materials have always been topics since the emergence of quantum theory. This has encouraged physicists to bring up ideas such as Low Energy Electron Microscopy (LEEM) and Photo Electron Emission Microscopy (PEEM) to image materials with low dimensionality[2]. Yet some 2D materials are very sensitive to radiations due to their low dimensionality, D. Geelen *et al.* developed electron-Volt Transmission Electron Microscopy (eV-TEM)[5], which could be a potential method to image radiation-sensitive 2D materials without much damage.

Unlike conventional EM, the landing energy of incoming electrons in LEEM and eV-TEM is typically 4 to 6 orders of magnitude smaller, and it lies between 0 and 100 eV in general[2, 6]. Especially for a landing energy below 30 eV, the incoming electrons are barely able to create excitons

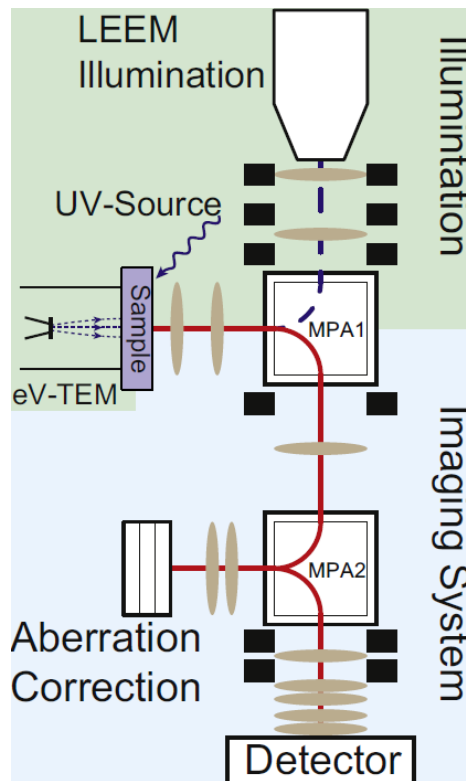


**Figure 1.1:** Configuration of ESCHER, figure is taken from [5].

or plasmons in thin samples, which increases MFP of electrons and thus allows high electrons transmission rate[5, 6]. Hence, the increasing MFP at lower energies, as is described in the “universal” MFP curve, can still provide us with atomic resolution[1] with minor sample damage[6].

In the previous study by Geelen *et al.*, a combination of LEEM and eV-TEM was used to measure both inelastic mean free path (IMFP) and elastic mean free path (EMFP)[1]. In that experiment, eV-TEM has proven itself to have a clear potential in determining the MFP’s. In our lab, we are using ESCHER[7] (set-up is shown in Figure 1.1) to probe the MFP’s of samples in UHV. In both LEEM and eV-TEM experiments, we are using varying landing energies of electron beams to probe the total MFP of the sample. As indicated in Figure 1.1, the detector detects the intensity of electron beam from reflectance in LEEM mode whereas the eV-TEM probes from the transmission of the beam. In general, the reflectance should increase when the landing energy of the electrons does not match with the band structure of the sample since existence of electrons at such energies inside the sample would be prohibited. And thus the transmission would

decrease since the incoming electrons cannot propagate through the sample, and *vice versa*. Hence, it is expected that there should always be a dip(peak) in eV-TEM curves in correspondence to a peak(dip) in LEEM.

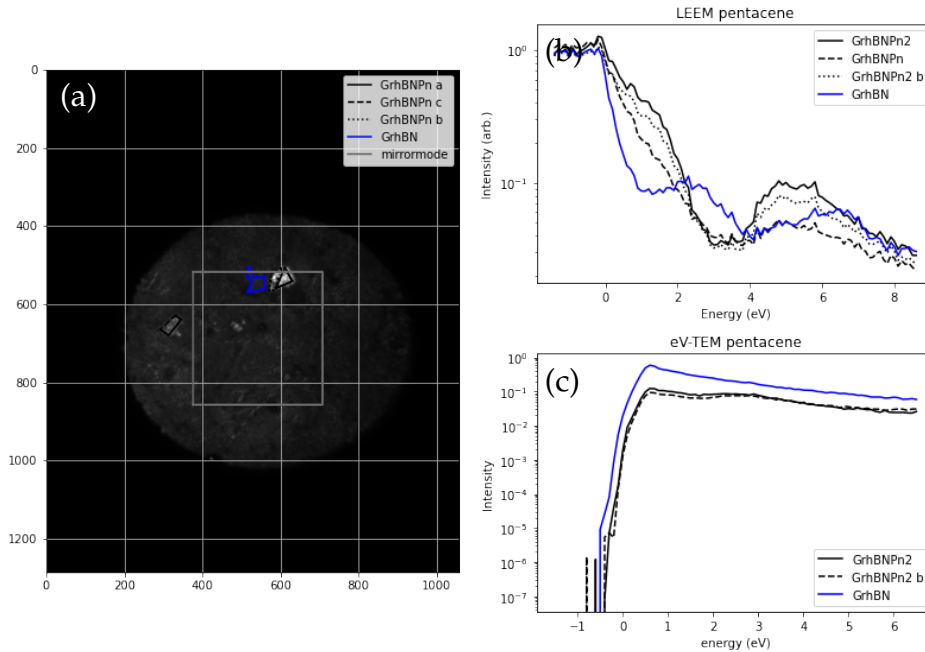


**Figure 1.2:** (a) LEEM image of the stacked sample of graphene, hBN and pentacene crystalline, intensity curves from (b) LEEM and (c) eV-TEM were measured on different spots indicated in (a). Figures offered by Leander Kalff.

In recent experiment by Neu *et al.*, a newly developed eV-TEM has already exhibited high spatial resolution less than 10 nm, which can be applied to image samples of tens of nanometers in size[6]. However, that eV-TEM resolution is still much larger than the theoretical resolution limit[6]. As is shown in Figure 1.2(b), the LEEM curve of graphene-hBN (plotted in blue) has distinguishable peaks at around 2 eV and 6 eV, however there is no clear sign of corresponding dips in the eV-TEM curves (shown in (c)). Hence it is very likely that the spread of energy in eV-TEM is too large and thus it eliminates the peaks and dips. The disappearance of dips and peaks may be caused by considerably large energy spread and low spatial coherence of the electron beam[6]. Thus to improve the resolution of eV-TEM, a new configuration of eV-TEM with better collimated electron beam is needed.

In this thesis, we will introduce a new configuration of eV-TEM, which is aimed to improve both energy spread and spatial coherence at the same time by replacing the thermal emission tip to a field emission tip. Some

background theories will be briefly introduced in Chapter 2. Then we will focus on the new design of eV-TEM, namely the geometry of the eV-TEM gun and the corresponding voltage configuration for the best beam collimation in Chapter 3. After electrons transmit through the TEM-grid, we need to normalize the current density based on the current density transmitted through empty holes of the TEM-grid. However, the current density through the hole is not consistent with different landing energies due to lensing effect. In Chapter 4, we will set up another model to find out how lensing effect will influence the probing results.

## Background

As we plan to replace the electron source with a field emission tip, which has a different size and operation principle from the thermal emission tip we are currently using in the lab. Hence changes in the electron optics will be necessary, to ensure best collimation. And we will use electrostatic lenses to collimate the electron beams in this project.

### 2.1 Electrostatic Lens

The working principle for optical lenses has been well studied since humans started to make prescription lenses for better eye sight. By inserting certain transparent materials on the optical path, the light can be deflected. If we can arrange the configuration of the geometry properly, we can have a focus vision of the objective we want to observe.

However, it is rather hard to apply the identical method to electrostatic lenses because they are using electrons instead of photons for probing. But based on the same idea, we can image the samples from electron beams by altering the "refractive index" of the medium through which the electrons travel.

Since forces are applied to electrons when traveling in an electric field, electrons can be accelerated or decelerated in the field. Hence it is possible to create a certain field in which the trajectories of electrons can be calculated analytically so that we are able to design the lens to meet our requirements[8].

Figure 2.1 shows an example of an electrostatic lens called einzel lens. In the einzel lens, the field is generated by putting three electrodes (shown in Figure 2.1(a)) with a spacing of 2 cm at different potential values. In this

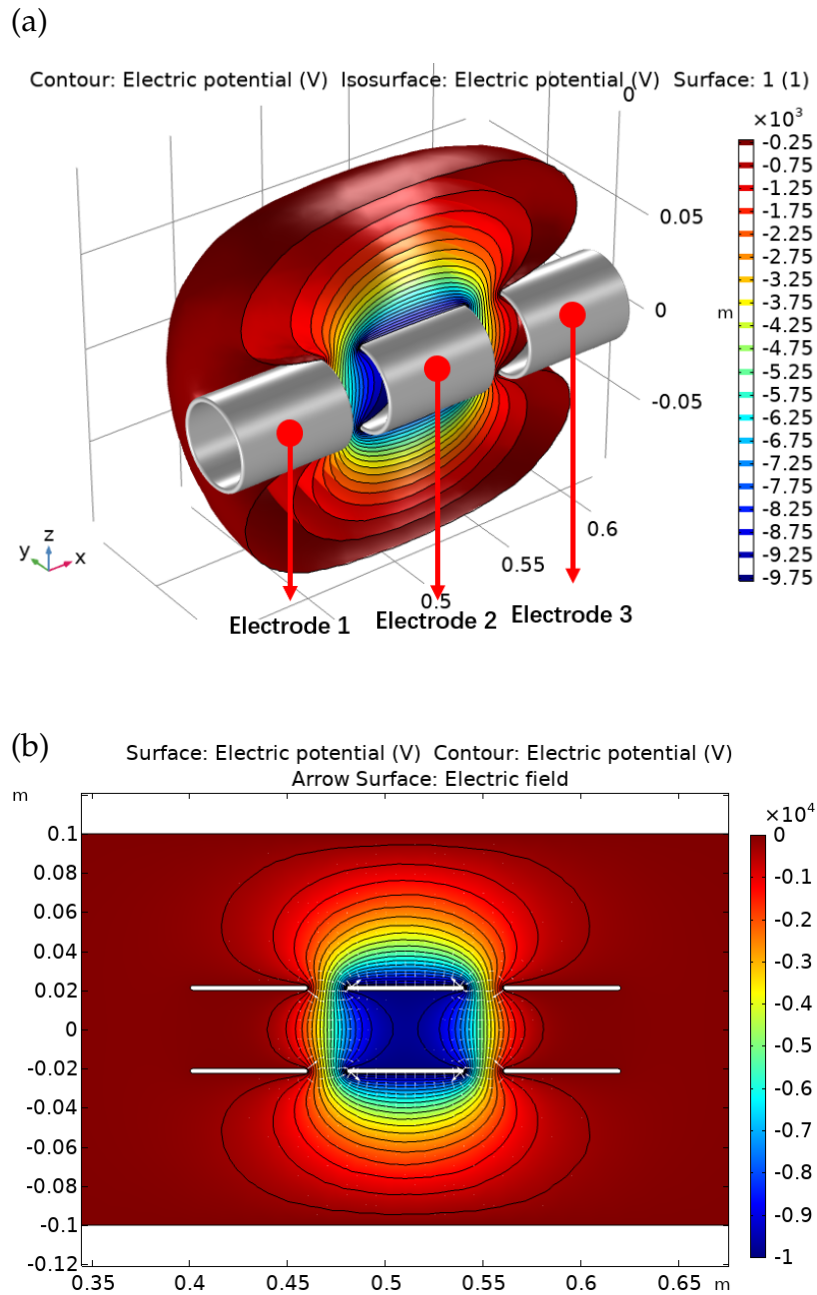


**Figure 2.1:** (a) 3D and (b) 2D contours of the field in an einzel lens, the color legends indicate the potential values. Simulations and plots are generated from COMSOL.

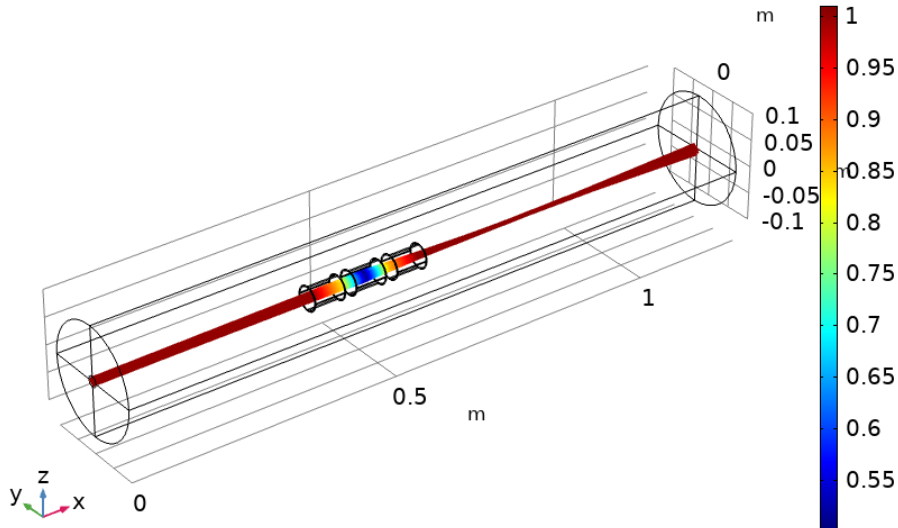


**Figure 2.2:** Trajectories of electrons traveling through the einzel lens. The legend bar indicates the portion of kinetic energy with respect to the initial kinetic energy of the electrons. There is a clear beam waist at around  $x = 0.8m$ .

example, the electrons have a high initial kinetic energy of 20 keV, the field in between the electrodes must be strong enough so that electron trajectories can be "bent" more noticeable based on the theorem of momentum. In this example, we ground Electrodes 1 and 3 and set Electrode 2 at -10 kV, which will only allow electrons with kinetic energies larger than 10 keV to pass through. This can create a strong field in space, especially in between the electrodes where electrons will pass through.

Figure 2.2 shows the trajectories of the electron beam. The kinetic energy shown in the figure indicates that the electrons are decelerated first when entering from Electrode 1 to Electrode 2, then they are accelerated after Electrode 2. But since the equipotential surfaces are not perpendicular to the electron beam, electrons may feel the force in the  $y - z$  plane, i.e. they may have transverse velocities after collimated by the einzel lens. This transverse velocity will eventually "focus" the beam and form a waist which can be seen at around  $x = 0.8m$ .

From the einzel lens example above, we can build up our own electrostatic lenses by using electrostatic fields. However it is not enough to simply accelerate and decelerate the electrons to build an electrostatic lens, we must create an inhomogeneous field so that transverse velocities of

electrons may develop. Because the Lorentz force is always “transverse”, hence one could also use magnetic field to build up a lens for electron beams.

On the other hand however, the existence of an inhomogeneous field may also give rise to problems. In the ESCHER configuration, there is a LEEM electrostatic lens with an electric potential of around 15 kV near the sample. As the sample is placed on a TEM-grid which has an array of holes, electric field may “leak” into the holes hence create an inhomogeneous field near the TEM-grid. In the TEM experiments, electrons may thus experience the inhomogeneous field. As a result, some electrons that should hit the TEM-grid will be accelerated and go through the holes. This unwanted phenomenon is called the lensing effect, and it will increase the beam intensities in a noticeable way. We will go into more details about it in Chapter 4.

## 2.2 Field Emission

In previous work by D. Geelen and P. Neu *et al.*, a thermal emission tip was used in the eV-TEM[6]. However, thermal emission tips can usually give a wide energy spread of several electron volts[9], which decreases the energy resolution in the MFP probing experiments.

Figure 2.3 shows how the Fermi-Dirac (FD) distribution changes as the temperature changes. By heating up the thermal emission tip, we can “flatten” the FD curve and electrons can gain thermal energies to exceed the work function of the tip, which enables them to have enough kinetic energy to escape from the tip. Since we usually heat the tip above 1000 K, the FD curve can be very flat and thus electrons with a wide range of energies can escape from the thermal emission tip. Such wide range of energy can thus give low spectral resolution in the end. Another drawback of thermal emission tip is that it has a large emission area, which makes the brightness of the tip very low[9].

To have a more monochromatic and brighter electron emission gun, we need to substitute with a cold field emission (FE) gun in the eV-TEM. Different from thermal emission gun, a cold FE gun does not need high temperature to drive electrons out. Instead, it is using the quantum tunnelling effect. Figure 2.4 shows the potential barrier of field emission in a bulk metal emitter[11]. By applying a high voltage drop outside the emitter, electrons may have a higher chance to tunnel through the barrier and escape into free space. To increase the current intensity, i.e. number of electrons emitted, a greater electric field may be applied. This makes the

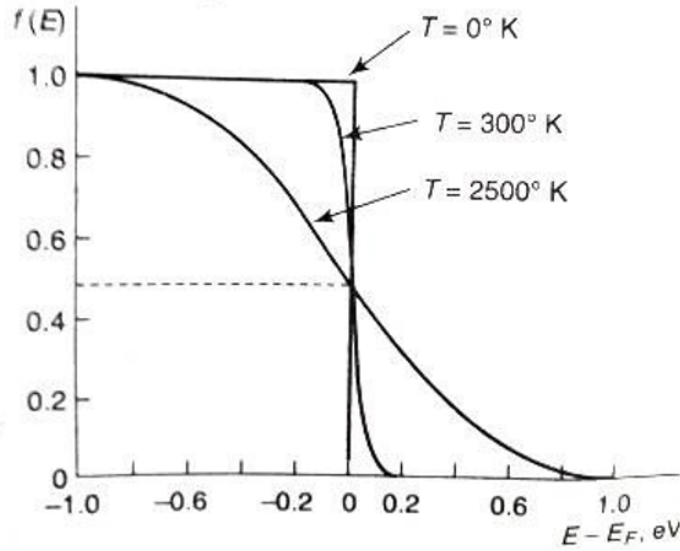


**Figure 2.3:** Fermi-Dirac distribution as a function of energy. The curves are plotted at various temperature ranges:  $T = 0\text{K}$ ,  $T = 300\text{K}$  and  $T = 2500\text{K}$ . At  $T = 0\text{K}$ , the FD distribution function has a step-like characteristic. Figure taken from [10].

slope of  $V(z)$  larger and hence narrower potential barrier:

$$J_{FN}(F) = A\phi^{-1}F^2e^{-B\phi^{3/2}/F} \quad (2.1)$$

where  $A = e^3/8\pi h$  is the first Fowler-Nordheim constant and  $B = 8\pi\sqrt{2m_0}/3eh$  is the second Fowler-Nordheim constant.  $F$  is the magnitude of electric field and  $\phi$  is the work function of the metal. Equation 2.1 is known as the elementary Fowler-Nordheim equation[11]. Even though Eqn 2.1 may need adaptations to describe the field emission from highly-curved FE tips[11] as we are using a FE tip with radius of  $R = 100\text{ nm}$ , it is still sufficient to get an intuition from Eqn 2.1 that higher electric field does help to increase the current intensity.

Since the transmission rate of electrons decreases exponentially as the energy difference increases, this may guarantee a much narrower energy spread compared to the thermal emission. In fact a FE gun can provide electron beams with an energy spread of a few tenths of an electron volt as well as an emitting area less than  $10\text{ nm}^2$ [9]. Besides, it also has a high brightness, which is about three orders of magnitude higher than that of conventional thermal emission guns[9].

There is another factor of field emission we should consider in this experiment. As we have only discussed energy spread in FE guns above, the directions of outgoing electrons however may not be perpendicular to

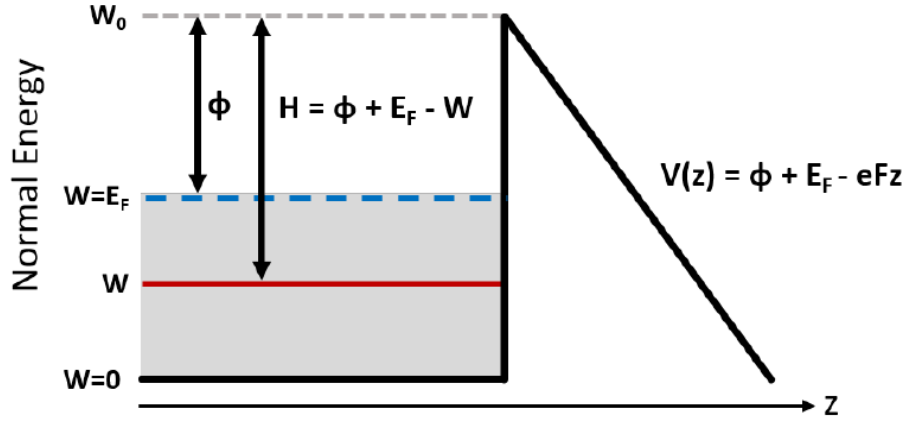


**Figure 2.4:** A schematic diagram of potential barrier in a planar FE emission. The work function is denoted as  $\phi$ ,  $F$  is the magnitude of electric field and the triangular potential barrier is defined by  $V(z)$ . Figure is taken from [11].

the emitting surface. Hence it may be problematic to run simulations afterwards as we could only set one specific direction for all electrons on a spherical surface in COMSOL simulation.

Figure 2.5 shows the angular spread of the outgoing electrons. In this model, the metal tip with a radius of  $R_0$  is placed at a distance of  $L$  away from a flat screen. The flat screen has a fixed voltage  $V_0$  which generates an electric field around the tip. Then the field  $F_0$  at the tip apex is given by[12]:

$$F_0 = \frac{V_0}{kR_0}, \text{ with } k \simeq \frac{1}{2} \ln\left(4 \frac{L}{R_0}\right) \quad (2.2)$$

Assume that the curvature of equipotential surface corresponding to the work function  $\phi$  outside the tip is much smaller than  $R_0$ , i.e.  $\phi/F_0 = \Delta s \ll R_0 \ll L$ [12]. Then the beam opening is given by[12]:

$$\Delta\theta_e \simeq 2\left(\frac{F_0}{\phi^{3/2}}\right)^{1/2} \quad (2.3)$$

and the half of the total angular width  $\Delta\theta_t$  is given by:

$$\Delta\theta_t \simeq \sqrt{\frac{\Delta E}{E_F}} \quad (2.4)$$

where  $\Delta E \simeq \frac{F}{\sqrt{\phi}}$  and  $E_F$  is the Fermi energy[12].

$\Delta\theta_e$  in Eqn 2.3 is defined as the angle between the normal to the tip apex and the normal to the equipotential surface[12]. It is clear that as the

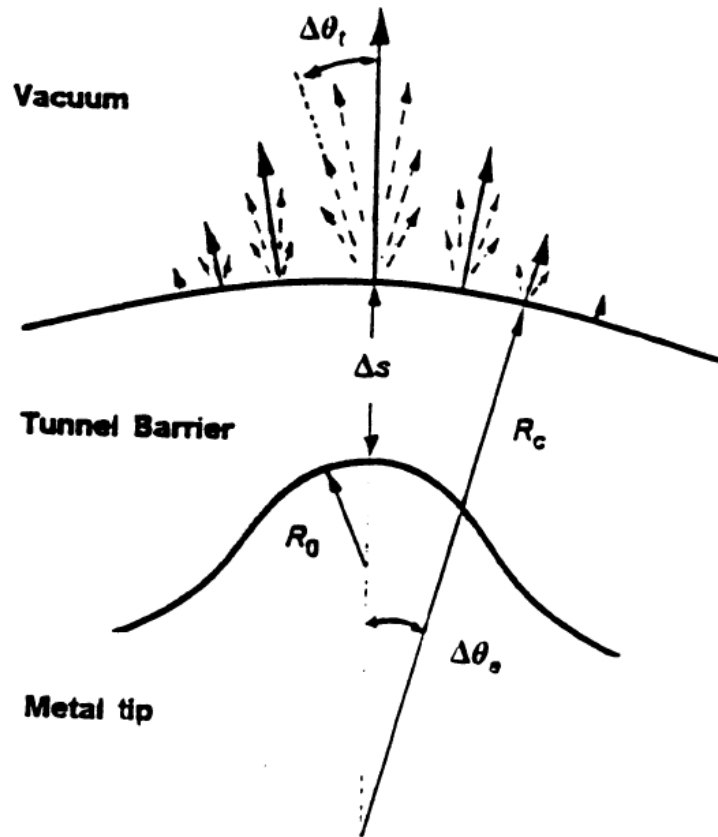


**Figure 2.5:** A sketch for field emission angular spread. The metal tip has a curvature of radius of  $R_0$ . The possible outgoing directions are plotted as solid and dashed arrows on the surface between the tunnelling barrier and vacuum.  $\Delta\theta_t$  denotes the half of the total angular width. Figure is taken from [12].

field increases, the outgoing angle decreases. Hence by applying a high voltage to the FE tip, we can confine the outgoing electron beam within a cone around the normal to the tip apex[12]. This can also give us an intuition of the most reasonable outgoing angle for our simulations.

## 2.3 Electron Microscopy

Inspired by einzel lens, E. Ruska *et al.* developed a new technique called transmission electron microscopy (TEM) in 1932, which was awarded with Nobel Prize in Physics in 1986[13]. The resolution of traditional optical microscopy is mainly limited by the wavelength of the light, which is too

large to visualize samples at atomic scales. This is characterized by what is now known as Abbe diffraction limit,

$$d = \frac{\lambda}{2n \sin \theta} = \frac{\lambda}{2NA} \quad (2.5)$$

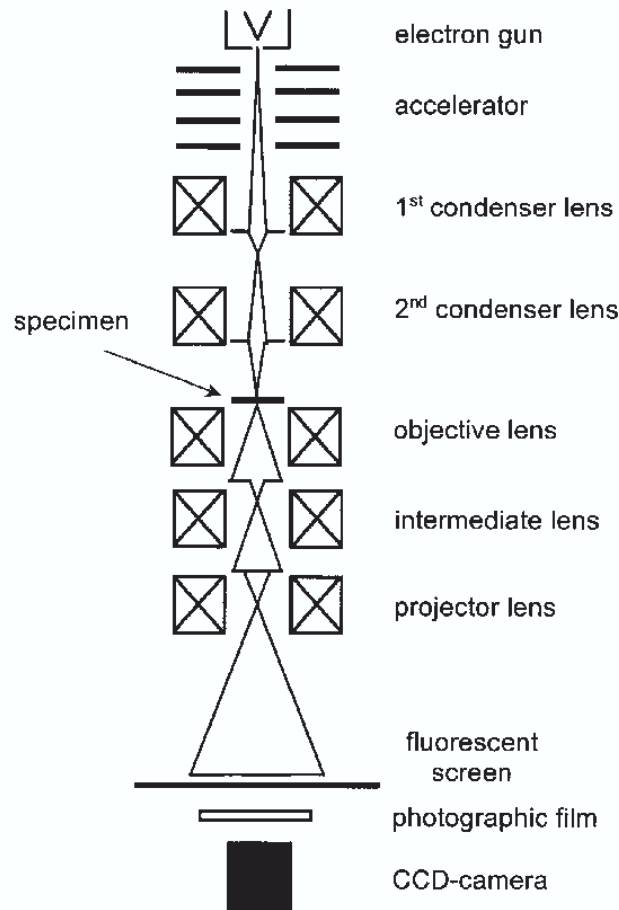
where  $d$  is the minimal spatial distance that an optical microscope can resolve,  $\lambda$  is the wavelength of the light,  $n$  is the refractive index of the medium,  $\theta$  is the half-angle of the spot and  $NA$  is the numerical aperture. As  $NA$  is limited within a range from 1.4 to 1.6 in general, the spatial resolution is mainly limited by the wavelength of the visible light. If we substitute the light source to electron emitter, however, the De Broglie wavelength of electrons may be several orders of magnitude smaller than the optical wavelength that is determined by the kinetic energy of the electron, suggesting a much finer spatial resolution. This method paved a promising way to probe samples at even sub-Ångstrom resolution[4].

Figure 2.6 shows how TEM probes the sample. The electrons are first extracted and accelerated from the electron gun. Before the electron beam probes the sample, a series of lenses are applied, which are usually operated by electric or magnetic field. This process is called collimation, and it is widely used to collimate the beam so that the electrons can project to the sample perpendicularly. After collimation, the beam with the information of the sample will be focused again by objective lenses and projected onto a fluorescent screen, converted to photonic signals and eventually recorded by a CCD camera[14].

However, such configuration has several drawbacks, one of which is aberration (Figure 2.7). There are three main causes of aberration in electromagnetic lenses, which are spherical aberration (Figure 2.7(b)), chromatic aberration (Figure 2.7(d)), astigmatism[15] as well as higher orders of aberration thereafter. In this chapter, higher orders of aberrations are neglected, and we will only focus on the first two types of aberration.

In practice, fields in electromagnetic lenses are much stronger near electrodes, and thus electrons may experience stronger fields and trajectories may bend heavier than they are expected. This is what we call spherical aberration. One way to overcome this problem is to add an aperture to block the electrons that are too close to the electrodes of the lenses (shown in Figure 2.7(c)). However, this method is negatively affecting the maximum resolution[15], as it is actually reducing the  $NA$  in Equation 2.5.

Another important part of aberration is known as chromatic aberration (Figure 2.7(d)). This is caused by the energy spread of the incoming electrons. Electrons with different energy spectra would be collimated by the field differently and eventually have different focal points, which is also



**Figure 2.6:** Typical schematic of a TEM, figure taken from[14].

widely seen in optical systems. There are two ways to reduce such negative impact: 1) Change the current configurations of electron microscope (EM), which allows an aberration-correction procedure, one example is the aberration corrected LEEM[2] in ESCHER[7]. 2) Substitute to a more coherent electron beam source, which gives rise to the use of field-emission gun. This can effectively reduce the chromatic aberration.

### 2.3.1 LEEM and eV-TEM

R. Tromp *et al.* introduced one way to allow aberration correction in a LEEM instrument (Figure 2.8(b)) in his published paper [2].

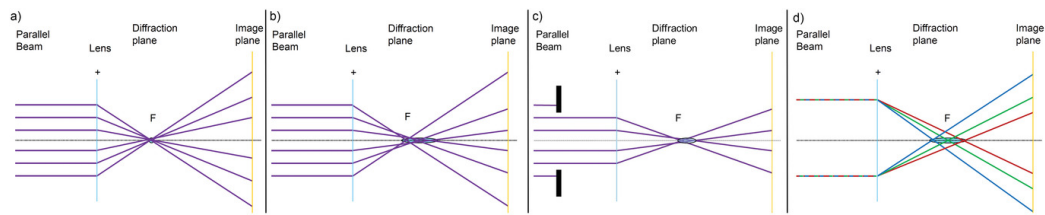


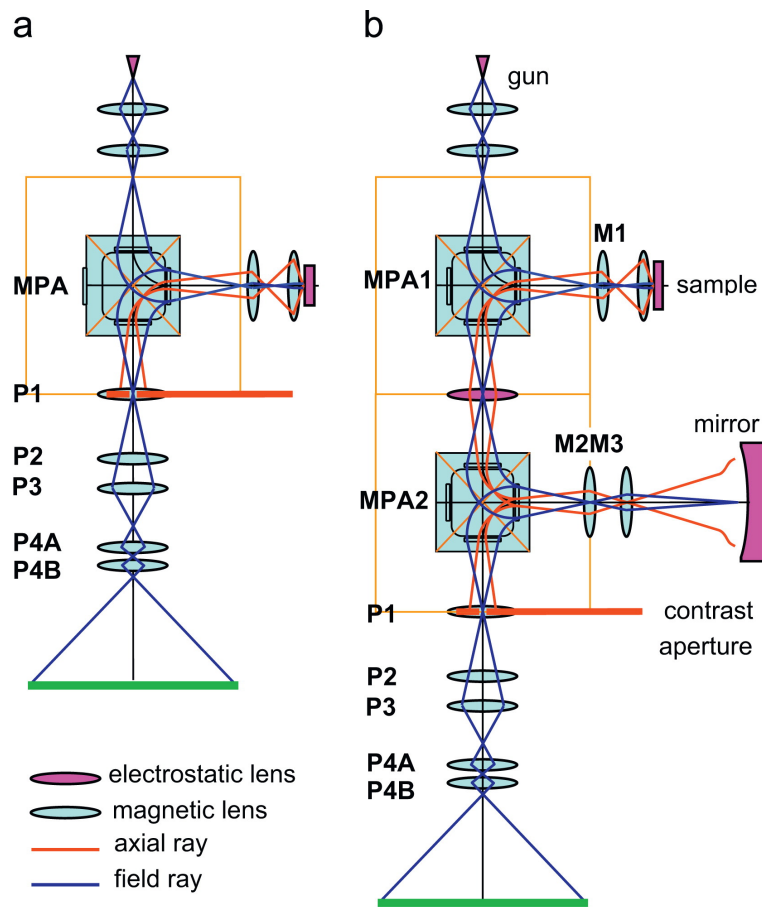
**Figure 2.7:** Sketches of aberrations in electromagnetic lenses. (a) A perfect lens that all electrons have a common focal point. (b) Spherical aberration (c) A  $C_2$  aperture can be added to reduce the spherical aberration. (d) Chromatic aberration. Figures taken from [15].

The LEEM in Figure 2.8(a) follows the same working principles as we have introduced previously (Figure 2.6), but it probes the samples by “reflections” with much lower electron energies, and thus a set of magnetic prism arrays (MPA) is needed. The probing energy is strictly defined by the voltage difference between the electron emitter and the sample[2]. However, this configuration is not able to correct aberrations. To correct aberrations caused by the objective lenses, R. Tromp *et al.* added another MPA after the beam is deflected from the first MPA (shown in Figure 2.8(b)) so that the beam can be deflected again by the second MPA to an electron mirror[2].

This new design of LEEM can effectively correct aberrations, suggesting the theoretical ultimate resolution down to 1 nm ( $E=30$  eV,  $\Delta E=0.25$  eV)[2]. And it has already been used in ESCHER in our lab[7].

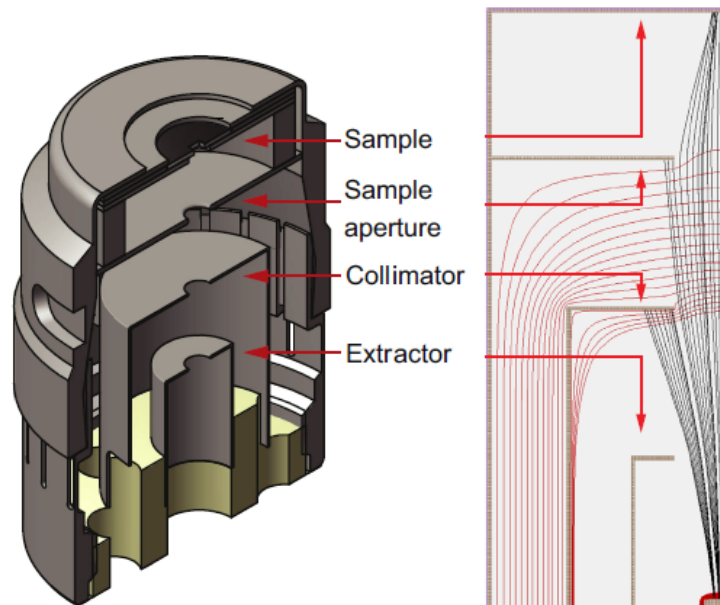
Apart from probing the samples via “reflection”, we can also use eV-TEM to visualize the samples in a “transmissive” way by emitting electrons from the back side of the samples (illustrated in Figure 1.1). This method can provide us with more detailed information about the IMFP and EMFP of the samples, revealing their spatial structures as well as band structures.

Figure 2.9 shows the configuration of the eV-TEM developed by D. Geelen *et al.*. This eV-TEM is consisted with four main parts, namely the emitter disk, extractor, collimator and sample. After the electrons are extracted from the emitter tip by a strong electrostatic field generated by the extractor, they are accelerated to the collimator. Both the electric field between collimator and extractor as well as sample aperture will form two electrostatic lenses which are to collimate the beam. Then the beam is then filtered by the sample aperture so that the velocities of electrons that pass through can be more perpendicular to the sample, and hence the spherical aberration can be reduced.



**Figure 2.8:** Schematic diagrams of (a) an uncorrected LEEM instrument and (b) an aberration-correction allowed LEEM system. Orange “boxes” around the MPA indicate the positions of symmetrically located diffraction planes. Image taken from [2].

However, this configuration still cannot reduce spherical aberration effectively. In earlier work by P. Neu *et al.*, they proposed to use a new configuration that the thin shells of electrodes were substituted to some long cylinder electrodes[6], which could filter out most electrons that are less collimated and hence reduce spherical aberration effectively. But that configuration still has a large chromatic aberration due to the use of thermal electron source[6]. To better eliminate chromatic aberration as much as possible as well as to improve resolution of spectra, we will substitute the thermal tip to a field emission tip, which is capable of providing more monochromatic electron beams.



**Figure 2.9:** A schematic diagram of eV-TEM by D. Geelen *et al.*[5]. The figure on the right is the 2D sectional view of the 3D gun model shown on the left. The red lines are plotted out as equipotential lines and the black lines indicate the trajectories of electrons.

### 2.3.2 Mean Free Path

To understand how we can probe the internal structures of the samples from MFP's, some basic concepts of MFP shall be introduced.

In many-body systems, particles may interact with each other and scatter. Between two incidents of collisions, the distance that the single particle travels is called free path. By averaging free paths of all the particles, we can then get a statistically meaningful value, which is called mean free path.

MFP is characterized by several factors. Having more particles crowding in the same area makes chances of collisions higher, hence systems with higher density would generally have shorter MFP. Temperature also plays an important role in MFP. As temperature is characterized by the intensity of thermal motions of particles in the system, higher temperature leads to more collisions as thermal motions become more violent, and thus makes MFP shorter.

In electronics, MFP is usually referred to the MFP of electrons. In classical theory, the microscopic mechanism of conduction is characterized by the transportation of electrons. Hence once we know the MFP of electrons,

the conductivity is known according to Drude theory:

$$\sigma = \frac{e\tau}{m} = \frac{el}{mv} \quad (2.6)$$

where  $\tau$  is the time of which the electrons travel along the MFP, also known as the mean free time,  $m$  is the mass of the electron,  $l$  is the MFP and  $v$  is the velocity of electrons. Such classical theory still works in quantum world to some extent, if we translate some classical concepts to quantum language:

$$\sigma = \frac{el}{m^*v_F} \quad (2.7)$$

where  $m^*$  is the effective mass of electrons, which is defined from band theory, and  $v_F$  denotes the Fermi velocity. We should notice, however, that Drude model is microscopically wrong, yet its results still work as a coincidence.

In quantum mechanics, conductivity is related to band structures of the samples. Hence, learning the MFP enables us to study the band structures of the samples. In previous studies on MFP in different samples, people have found a so-called "universal" inelastic mean free path curve (Figure 2.10)[16]. This universality proposed that IMFP is largely independent of materials, and the possibility of electron being scattered can be energy-dependent. In Figure 2.10, There is a minimum of the IMFP at around 50 eV[5], because electrons cannot create plasmons or excitons at lower energy and thus have longer MFP[6].

However, in a previous study by D. Geelen *et al.*, the MFP curve was found to be structure-dependent, i.e. it can be material-dependent[1]. In the few-layer graphene experiment, D. Geelen *et al.* found that the reflectivity as well as transmissivity depends on the number of graphene layers (Figure 2.11), which can be theoretically explained by using a Fresnel-based model[1]. As the reflectivity and transmissivity can be probed from elastic reflected and transmitted current intensities, which are given as

$$\begin{aligned} T &= \frac{I_{et}}{I_0} = e^{-d/\lambda_{tot}} \\ T + R &= \frac{I_{et}}{I_0} + \frac{I_{er}}{I_0} = e^{-d/\lambda_{inel}}, \end{aligned} \quad (2.8)$$

and the EMFP is given by

$$\frac{1}{\lambda_{tot}} = \frac{1}{\lambda_{el}} + \frac{1}{\lambda_{inel}} \quad (2.9)$$

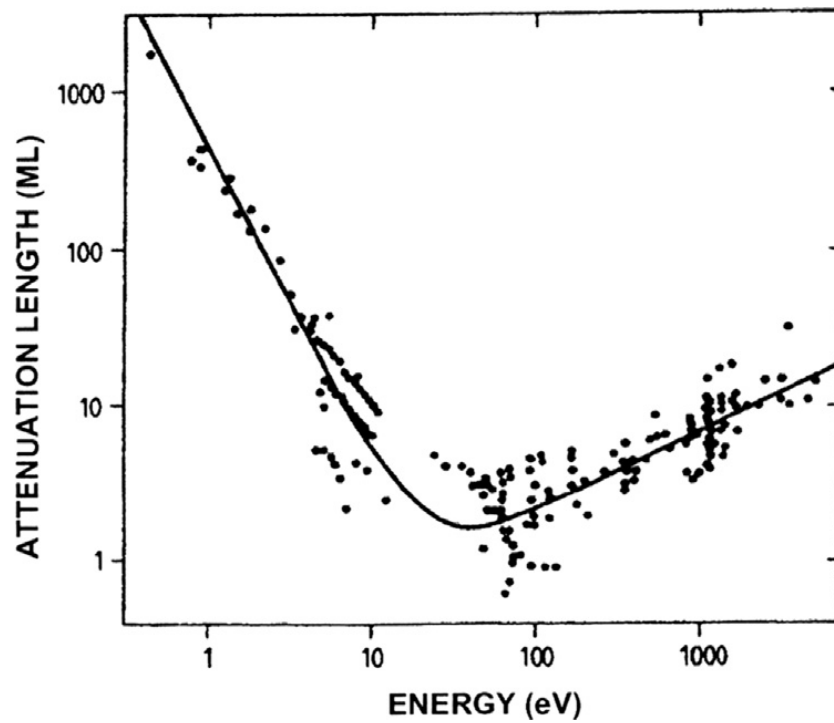


**Figure 2.10:** Universal inelastic mean free path curve, figure taken from [16].

we can acquire both the IMFP and EMFP from the combination of eV-TEM and LEEM experiments[1]. Figure 2.12 shows MFP curves plotted from the Eqns 2.8 and 2.8. The curves are decreasing in general, which is in agreement with the universal MFP curve in Figure 2.10. However, it is also obvious that these curves in Figure 2.12 have a finer structure, which show peaks and valleys. This proves that the MFP's depend on the number of graphene layers at low electron energy, yet the universality still holds on a large electron energy scale.

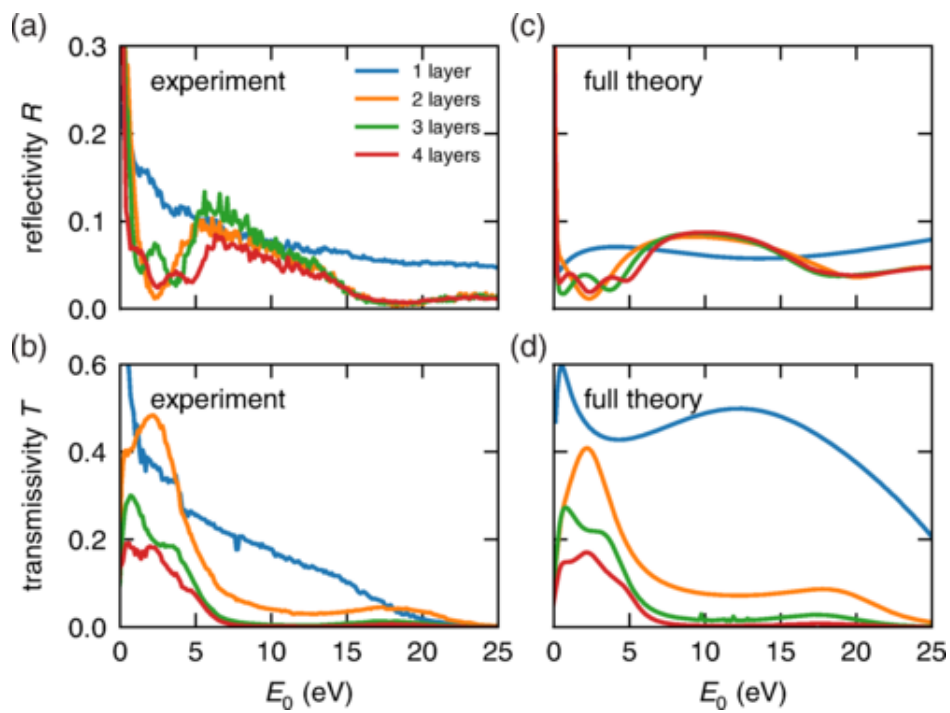


**Figure 2.11:** Reflectivity and transmissivity in units of graphene layers as a function of electron energy. Figure from [1].

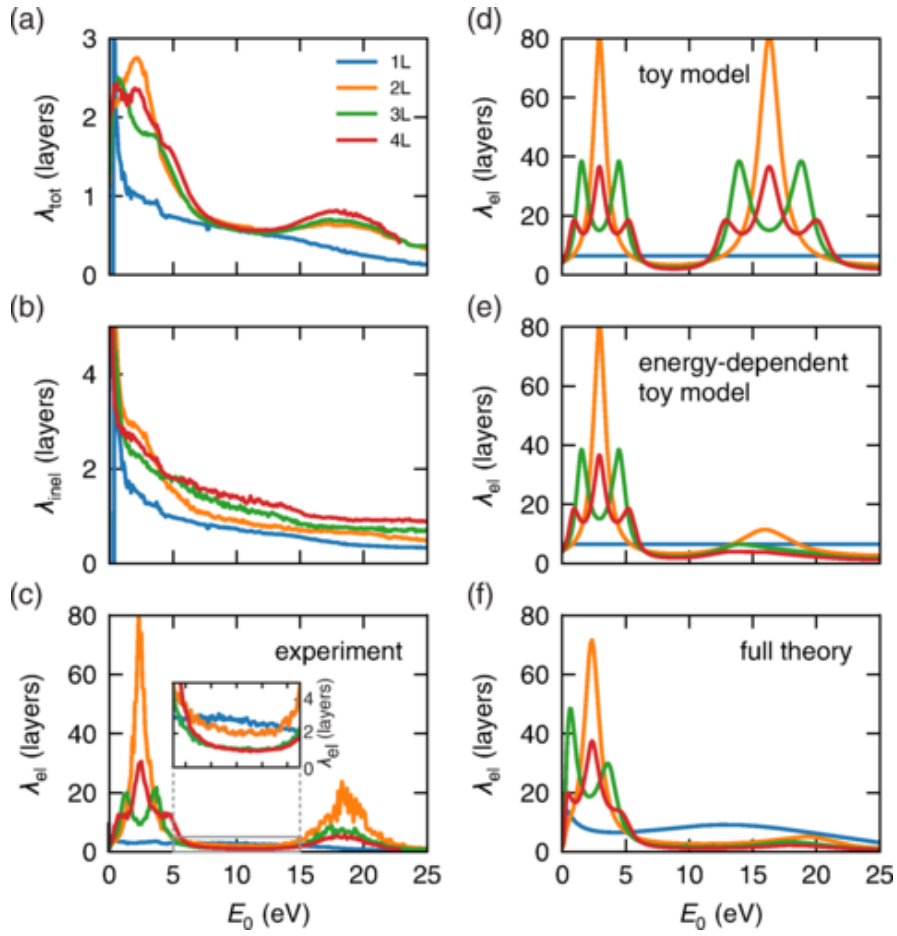


**Figure 2.12:** MFP measurements and their corresponding theoretical curves. All MFP's are plotted in units of graphene layers as a function of electron energy. Figure from [1].

## eV-TEM Gun

### 3.1 Methods

In this chapter, we will introduce how we set up the simulations for both eV-TEM and the TEM-grid. Geometries and voltage configurations of eV-TEM will be introduced in the first part. Geometries and simplification of the lensing effect in the TEM-grid model will be introduced in the second part. All simulations are run on *COMSOL 5.5* with packages for studies of electric fields and particle tracing.

#### 3.1.1 Geometry

Figure 3.1 shows the geometry of the eV-TEM in detail. The eV-TEM gun is cylindrically symmetric, hence we will simplify the geometry in 2D-axisymmetric form. The extractor is put at a high voltage of  $V_{ext} = 3$  kV so that electrons can be extracted and accelerated from the FE tip. The voltage of the sample cathode will determine the landing energy of electrons. In our lab, the voltage of the sample cathode is also determining the landing energy of electrons from the LEEM, hence we will put the voltage of the FE tip at a fixed voltage (grounded) without loss of generality. As we are only using low-energy beams in eV-TEM, hence the voltage of the sample cathode is put between 0 to 100 volts to determine the landing energies. The voltage of the collimator will be put between 100 to 1000 volts so that electrostatic lenses will be formed in the spaces between both extractor and sample cathodes and the collimator. We will mainly study the voltage of the collimator to optimize the electron beam so that it can give the minimum angular distribution at the TEM-grid for different landing energies.

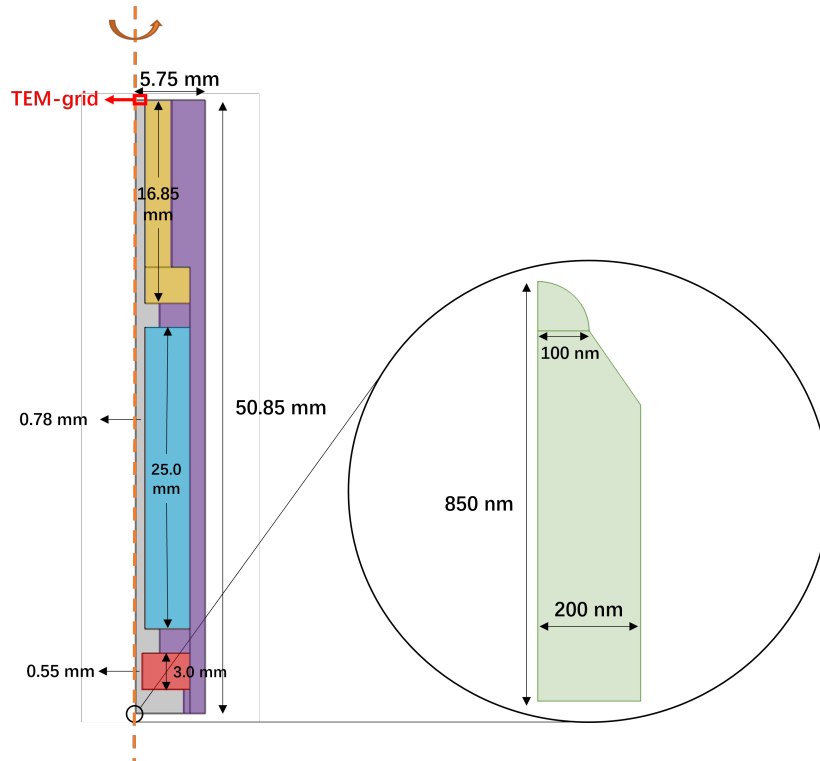


**Figure 3.1:** Geometry of eV-TEM in our simulations. Rectangular area painted in red is the extractor cathode. Blue area is the collimator cathode. Yellow area is the sample cathode. Purple area is filled with macor for isolation. Grey area is vacuum where electrons will pass through. The circle on the lower left corner is zoomed in and shown on the right-hand-side of the figure, this is the FE tip made from Tungsten. The small red box on the top is the TEM-grid where samples locate connected to the sample cathode. The red dashed line indicates the symmetric axis. All crucial parameters are labeled in the figure.

After setting up the geometries, we will create meshes to divide the whole geometry into small blocks so that electric fields can be studied by using differential equations. In this simulation, we are using triangular meshes. There are mainly three different sizes of meshes. In our eV-TEM, the FE tip is in nano-scale, and there is a 3 kV bias between the tip and the extractor, hence the electric field will be extremely large near the tip. In fact, the field at the tip surface can be as large as  $F \simeq 3 \text{ V}/\text{\AA}$ , thus we should handle the field carefully. In the mesh element creation, we generate the meshes near the tip with a maximum size of 20 nm and a minimum size of 0.1 nm. The second finest meshes are created in between the extractor, collimator and sample cathodes as the voltage drops by several

hundred volts in several millimeters. These areas have meshes in maximum size of 6000 nm and minimum size of 1 nm. Then the rest of the gun assembly has the coarsest meshes with a maximum size of 30  $\mu\text{m}$  and a minimum size of 1 nm.

While creating meshes, we noticed that the tip's geometry changes from the spherical shape to a triangular shape in the *Physics* module (Figure 3.2(a)). This is because the tip size is extremely small compared to the other parts of the eV-TEM, hence some resolution will be lost while presenting the geometry in the *Physics* module. In case this will also affect the studies on field geometry and particle tracing, we also plotted out the mesh and field geometries in Figure 3.2(b) and (c). Both the mesh and field geometries are spherical and in agreement with our assumption, hence the change of shape of the tip in the *Physics* module should not be problematic in our simulations.

### 3.1.2 Time Steps

Before running through simulations, setting reasonable time steps is also very important. Similar to the idea on choosing mesh sizes in the previous section, we should set time steps according to the particle velocity. In principle the time step  $\Delta t$ , particle velocity  $v_e$  and the mesh size  $\Delta l$  should satisfy:

$$\Delta t \cdot v_e \sim \Delta l \quad (3.1)$$

As each mesh element is considered as the minimum unit to store information of the electric field in the simulation. The time step should not be too large that electrons may be too fast to travel across the mesh elements while the interaction with the field may not be calculated. By setting a reasonable time step satisfying Eqn 3.1, we may minimize the calculation inaccuracies.

Hence, time steps should be small wherever the field changes sharply or the velocity is large. In our simulations, we are using the Runge-Kutta Dormand-Prince 5 algorithm as it will give the least calculation inaccuracies after comparing to simulation results by other algorithms. We set the total time that electrons need to travel from the FE tip to the TEM-grid to be  $t_0$ . Then we divide the whole trajectory into three main parts: 1) The electrons are emitted from the tip to the vacuum, time step is taken to  $\Delta t_1 = t_0 / (1 \times 10^{10})$  till  $t = t_0 / (2 \times 10^7)$  as the field is the largest near the tip. 2) After step 1, the electrons have already gained energy of  $\sim 1\text{keV}$ , hence the time step is taken to  $\Delta t_2 = t_0 / (1 \times 10^9)$  till  $t = t_0 / (1 \times 10^4)$  as the field is not as large as that near the FE tip. 3) After  $t = t_0 / (1 \times 10^4)$ ,

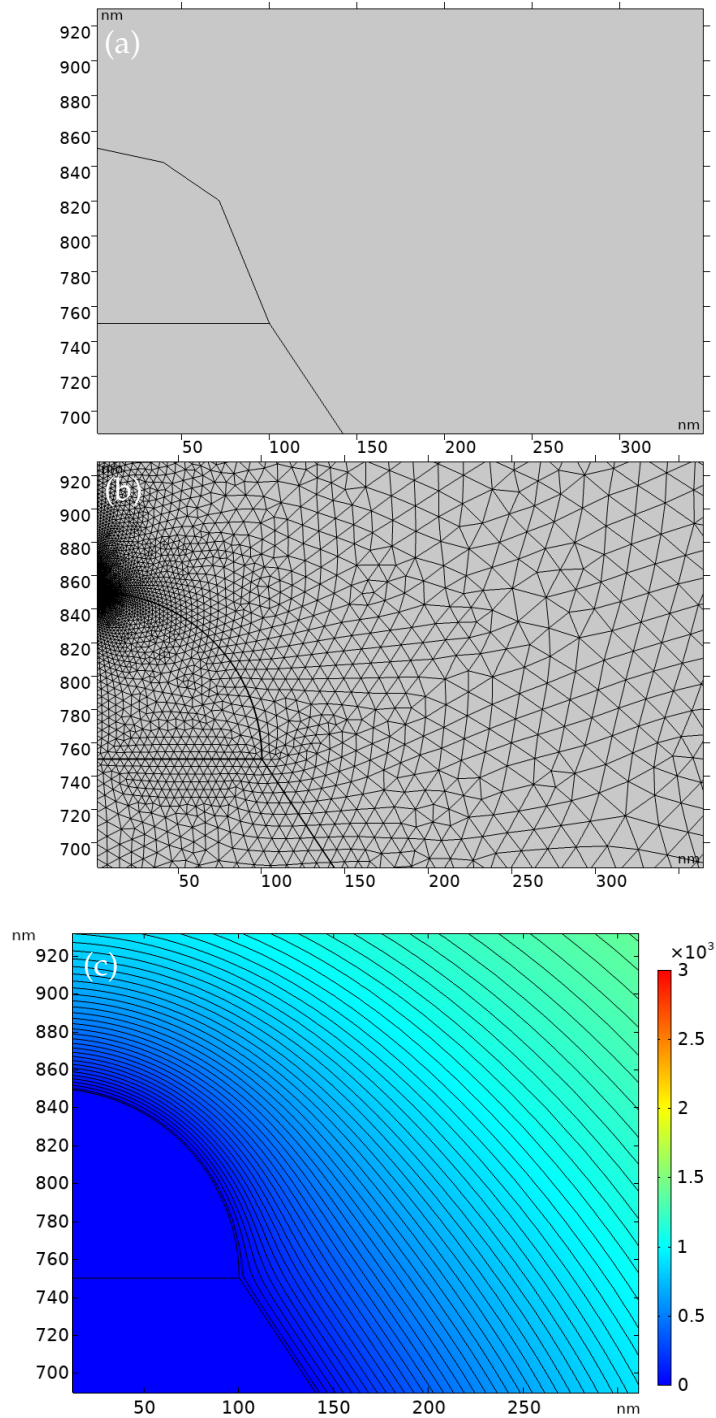


**Figure 3.2:** (a) Tip shape is shown as a non-spherical polynomial shape in *Physics* module. However, in (b) *Mesh* module and (c) calculated field, the tip as well as the field is in spherical shape.

the electrons will reach the collimator where the field is smaller than that near the FE tip, hence we will set the time step to  $\Delta t_3 = t_0 / (1 \times 10^5)$ .

Now, we need to determine the value of  $t_0$  as well as the initial time step for the initial condition. Since electrons are traveling with a vertical kinetic energy of more than 10 eV or an equivalent velocity of  $v_e = 1.88 \times 10^6 \text{ m/s}$  for the most of time, it is sufficient to narrow down the range of  $t_0$  to a reasonable value:

$$t_0 \simeq \frac{50.85 \text{ mm}}{v_e} \approx 3 \times 10^{-8} \text{ s} \quad (3.2)$$

In our simulation, the electrons have a initial kinetic energy of  $\sim 0.1 \text{ eV}$ , hence we set the initial time step  $\Delta t_0$  to  $1 \times 10^{-20} \text{ s}$  so that the initial positions of electrons are

$$v_e \cdot \Delta t_0 = (1.88 \times 10^5 \text{ m/s}) \times (1 \times 10^{-20} \text{ s}) \approx 1 \text{ fm} \quad (3.3)$$

away from the tip surface, which is still close enough to be considered to be at the tip surface.

### 3.1.3 Emission area

From Figure 3.2(c), the magnitude of electric field around the spherical tip is almost the same. Hence electrons from the FE tip should be considered at the first instinct as the potential distribution is the same around the tip giving rise to equal possibility of tunneling. However, it is hard to apply this condition to our simulations.

There are mainly two problems when using a uniform distribution of electrons on the surface. First of all, the electric field is nearly radial, hence electrons will be accelerated along the radial directions to the extractor. However, there is only a small opening for electrons to pass through the extractor, and most of the electrons will hit the extractor and disappear (shown in Figure 3.3). Since the algorithm we are using takes a huge amount of calculation power and time, those redundant electrons are of no help for our research and will also waste lots of calculation power and time. Secondly, as one can see from Figure 3.1, there is only a very small opening angle for electrons to reach the TEM-grid even if we do not collimate the beam. Hence using the realistic distribution of electrons will lead to a very limited number of electrons that reach the TEM-grid, which is not statistically significant as we need enough electrons to estimate the angular distribution of the beam at the TEM-grid. Hence we will only send electrons from a small area near the symmetric axis as they are the only

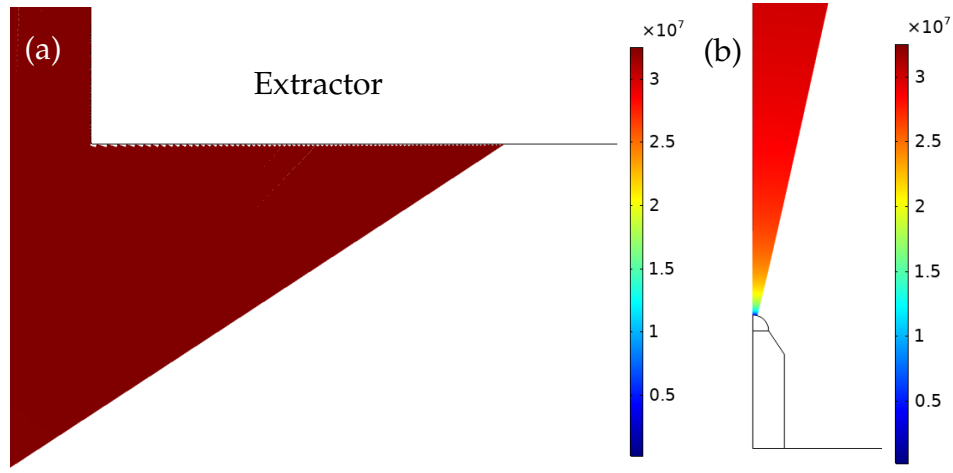


**Figure 3.3:** Electron paths near the FE tip. (a) Most electrons will hit the extractor and disappear. (b) Emission angle of  $25^\circ$  when most electrons can travel to the space between the extractor and collimator. Color bars indicate the kinetic energy of electrons. Color bars indicate the velocity of electrons in unit of m/s.

relevant portion. This will make simulations much more efficient without bias in the results as it is equivalent to increasing the number of electrons in practice.

As we can only set a fixed direction of initial velocities of electrons in *Particle Tracing*  $\Rightarrow$  *Inlet*, we need to specify a reasonable value for direction. In our simulations, we are using a Tungsten FE tip with radius of 100 nm, and the field  $F$  is  $3 \text{ V}/\text{\AA}$ . Hence we can get the beam opening angle from eq 2.3 that  $\Delta\theta_e \simeq 32.12^\circ$ . And angle spread is  $\Delta\theta_t \simeq 21.82^\circ$ . Hence, it would be reasonable to set the direction to be parallel to the symmetric axis, as the field is large compared to the initial energy and thus velocity is determined by the field after the first time step.

In combination with the previous discussions, it is practical and reasonable to emit the electrons with an initial velocity parallel to the symmetric axis from an opening angle of  $25^\circ$ .

## 3.2 Results and Discussions

We ran several simulations for various landing energies: 0.1, 1, 3, 5, 10, 15, 20, 25, 50 and 100 eV. At each landing energy, we also ran a sweep for various collimation voltage  $V_{col}$  to find the best collimated beam. Since there is an energy spread of around few tenths of electron volts in field emission, we will also check the influence of electrons with different initial

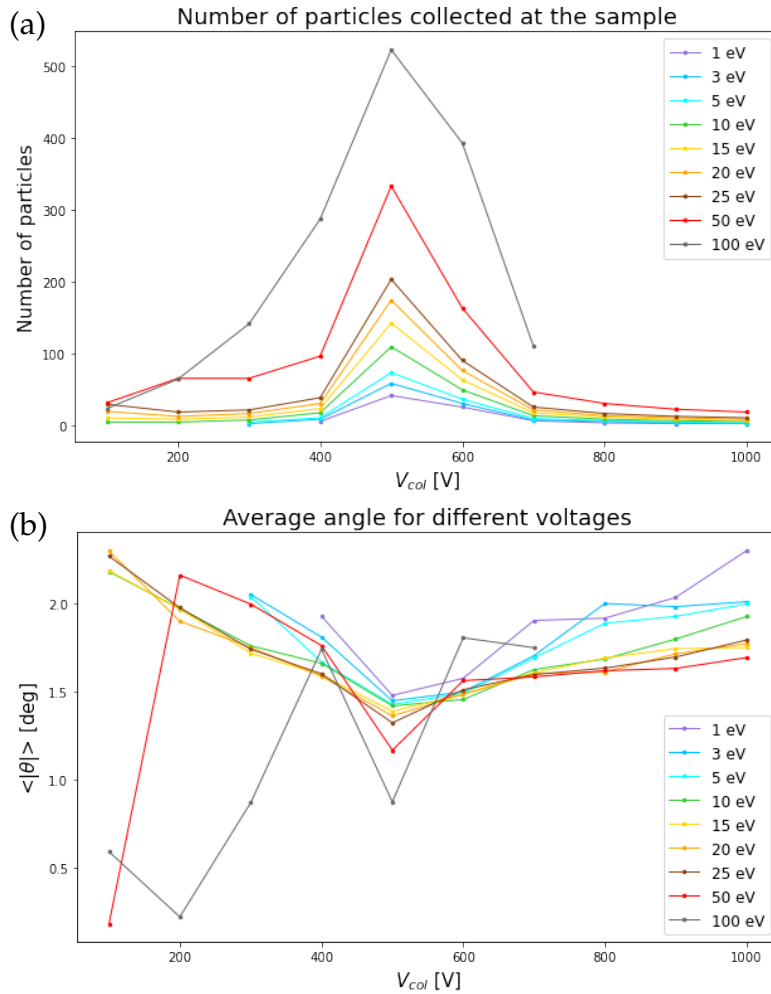


**Figure 3.4:** (a) Number of particles collected at the sample at various landing energies. (b) Average absolute angle as a function of collimation voltage  $V_{col}$ .

kinetic energies. For all simulations, the total number of electrons is 2000.

Figure 3.4(a) shows the number of electrons that are collected at the sample. It is very clear that there is always a peak of electron number at a collimation voltage around 500 V. This shows that we can expect the highest current density at such collimation voltage. It is also clearly shown in the figure that as the landing energy increases, more electrons will be collected at the sample. Since the electric field configuration below the collimator remains almost the same as the voltages between the FE tip, extractor and collimator are fixed, this implies that the electrostatic lens between the sample and collimator is playing a major role in changing the current density.

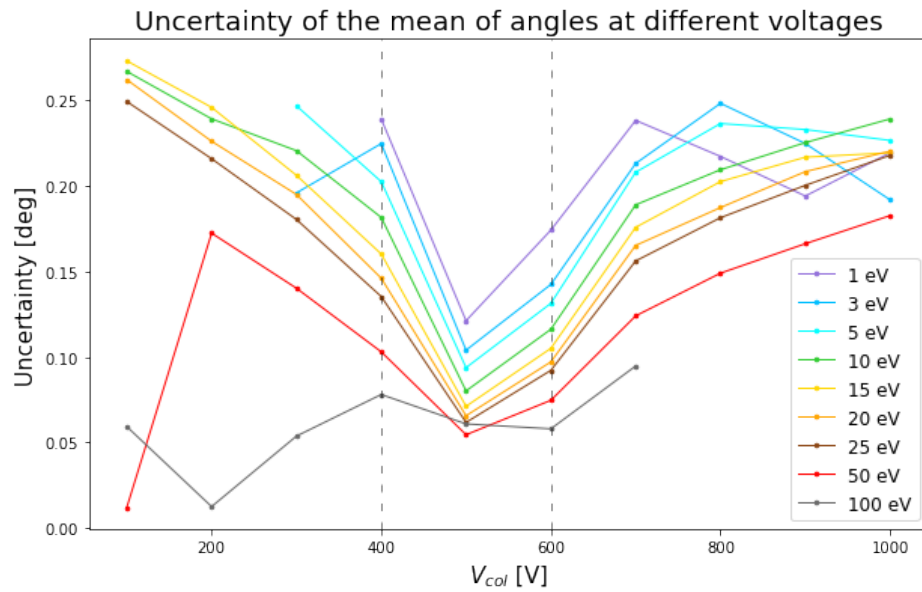


**Figure 3.5:** Uncertainty of the mean of angles at different collimation voltages. Black dashed lines indicate the collimation voltage range where statistically sufficient electrons are collected.

To determine how good our eV-TEM collimates the beam, we need to consider the spread of angles. The angle is defined as the angle between velocity and the symmetry axis. If the transverse portion of velocity is pointing to the right, then the angle is positive, and vice versa. The reason for our taking the average of absolute angle instead of the absolute of averaged angle as our criterium is that the whole geometry of eV-TEM is cylindrical symmetric. The negative angles will also have a corresponding mirrored positive angle in the mirror geometry due to cylindrical symmetry. Hence by taking the absolute values of angles first, the symmetry can be taken into account. Figure 3.4(b) shows the average of absolute angle. Apart from high landing energies ( $\gtrsim 50$  eV), all beams are also best collimated at 500 V. There is one more fact we should notice - the number of electrons collected at lower landing energies at other collimation voltages can be statistically insufficient, hence we should not trust the statistical values of them even if they have lower average of absolute angles.

Interestingly, at landing energies of 50 and 100 eV, there are still several tens of electrons collected at the sample, which in principle is statistically sufficient. Yet, the beam is best collimated at  $V_{col} = 100$  V for landing energy of 50 eV and at  $V_{col} = 200$  V for landing energy of 100 eV. The corresponding average of absolute angles are about half of that at  $V_{col} = 500$

V, which seem to be better choices of collimation voltage. But due to low current density, the image we can visualize in the end may be very dim. Hence, we would not suggest to collimate the beam at those collimation voltages, except that we can extend the duration time of exposure to increase the intensity, which will make the measurements less efficient.

Figure 3.5 shows the uncertainty of the mean of angles  $s$ , which is defined as

$$s = \sqrt{\frac{1}{N-1} \sum_{i=1}^N (\theta_i - \bar{\theta})^2}, \quad (3.4)$$

where  $N$  is the total number of electrons collected for each collimation voltage. For low energies ( $< 30$  eV), angle uncertainties around  $V_{col} = 500$  V are almost the lowest around  $0.1^\circ$  independent of changes of the collimation voltage. This suggests that  $V_{col} = 500$  V is ideal for beam collimation while also high current intensity.

In order to find out the best voltage configuration for the beam collimation,  $V_{col}$ , sweeps with smaller sweep steps were also studied. Figure 3.6(a) shows the total number of collected electrons at the sample. It is clearly shown in the figure that the highest current intensities, i.e. maximum number of collected electrons, do not share the same  $V_{col}$  as the landing energy changes. The collimation voltage when current density takes the maximum is gradually increasing as the landing energy increases, yet it still lies in a range from 530 to 570 V.

Figure 3.7 shows the uncertainty of the mean of angles of the angles shown in Figure 3.6(b). From Figure 3.7, the minima of the average of absolute angles are statistically significant.

From the discussions above, it is clear to see that for a certain geometry of eV-TEM gun, the collimation voltage is approximately identical for electron beams with a various range of landing energies. This is very promising as we do not need to adjust the voltage configuration frequently to collimate the beam, which can make the measurement efficient.

Aside from the general selection of collimation voltages for various landing energies, it is also interesting to look at collimation voltage around 200 V at landing energy of 100 eV (Figure 3.4). Figure 3.8 shows that the average of absolute angles takes a minimum at  $V_{col} \simeq 220$  V and that for the uncertainty of the mean of angles takes place at  $V_{col} \simeq 210$  V. Since both collimation voltages correspond to roughly the same current density and uncertainty of the mean of angles, it is sufficient to choose collimation

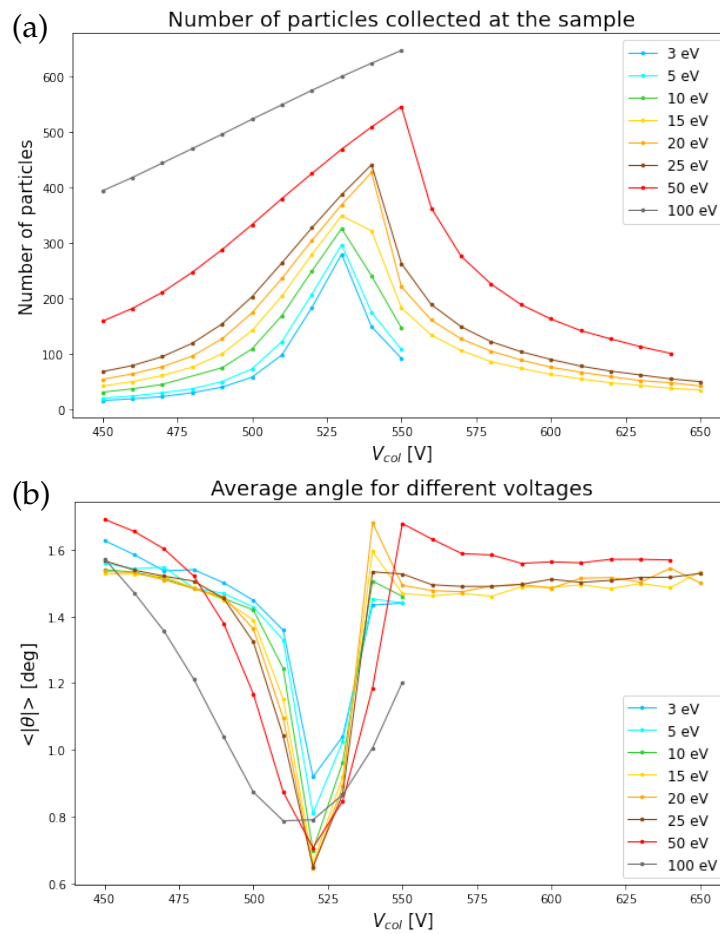


**Figure 3.6:** (a) Number of particles collected at the sample at various landing energies. (b) Average absolute angles of the electrons at various landing energies. Both figures show the sweep for collimation voltage  $V_{col}$  around 500 V with a smaller sweep spacing (10 V).

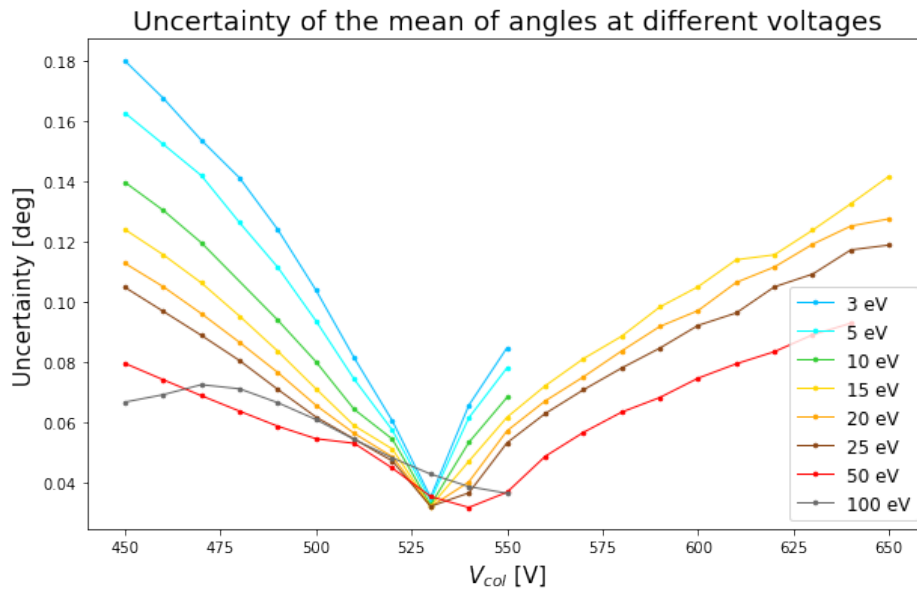


**Figure 3.7:** Uncertainty of the mean of angles at different collimation voltages with a smaller sweep step (10 V).

voltage of  $V_{col} = 220$  V if we were to run TEM measurements for extremely high energy resolution at landing energy of 100 eV.

We are also interested in the angle distribution of electrons collected along the sample. This can possibly help us to add a angle filter to get electrons with small angles. In principle, electrons which are traveling with smaller angles with respect to the symmetry axis should reach the sample electrode closer to the symmetry axis as a result of symmetric geometry of the eV-TEM gun. Figure 3.9 shows the angle distributions for three different landing energies. It is clearly shown that for various landing energies, electrons that land near the sample electrode have smaller angles. Hence we can also add a filter at the center of the sample electrode to only collect electrons with small angles and thus improve the collimation quality. Yet such method will still decrease the current intensity significantly.

### Different Initial Kinetic Energies

In field emissions, there will always be an energy spread of several tenths of eV[9]. Hence it is necessary to study how the initial kinetic energies will influence the angle distribution of electrons.

Figure 3.10 shows two extremes of voltage configurations. For landing energy of 1 eV, we can only choose  $V_{col} = 500$  V since only such voltage

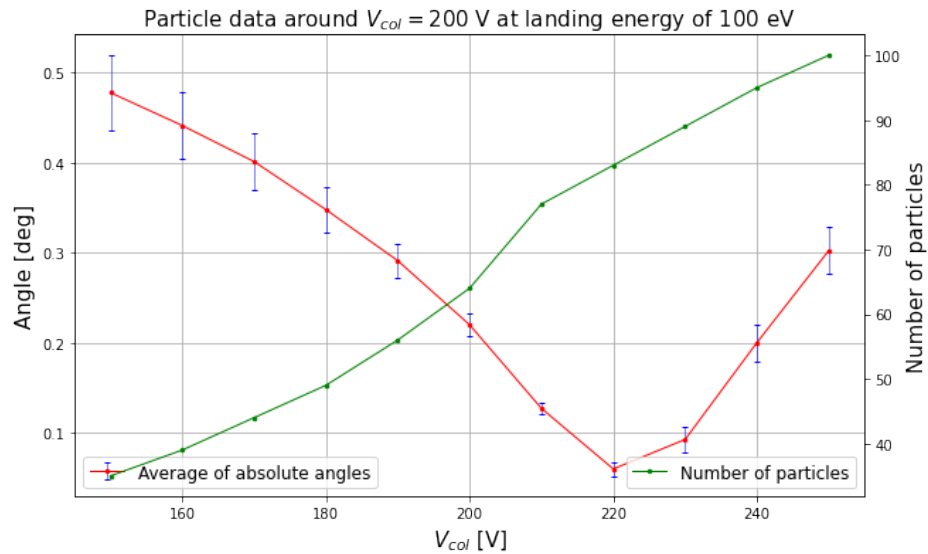


**Figure 3.8:** Average of angles (red), uncertainty of the mean of angles (blue) and number of electrons collected at the sample (green) at collimation voltage around 200 V at landing energy of 100 eV.

configuration allows the most electrons to reach the sample. Since initial kinetic energies are compatible to the landing energy, this can help us to see if initial kinetic energies will influence the angle of electrons significantly. For a landing energy of 100 eV, we set  $V_{col} = 200$  V because all angle data show minimum spread around this voltage configuration yet there are still sufficient electrons collected at the sample. This voltage configuration allows us to see if angles change for high-quality collimated beams.

It is obvious from the figure that for all five different initial kinetic energies, the total number of electrons collected at the sample is almost the same. Most importantly, the averaged values of absolute angles are barely influenced by the change of the initial kinetic energy. Hence, the energy spread of FE tip will not influence the collimation quality in a noticeable way. Therefore only considering one initial kinetic energy will be enough to study the collimations.

### Computation Inaccuracies

In the simulations, computation inaccuracies are inevitable. Figure 3.11 shows the simulated landing energies of electrons. In principle, all data points should fall on the dashed lines as a result of energy conservation.

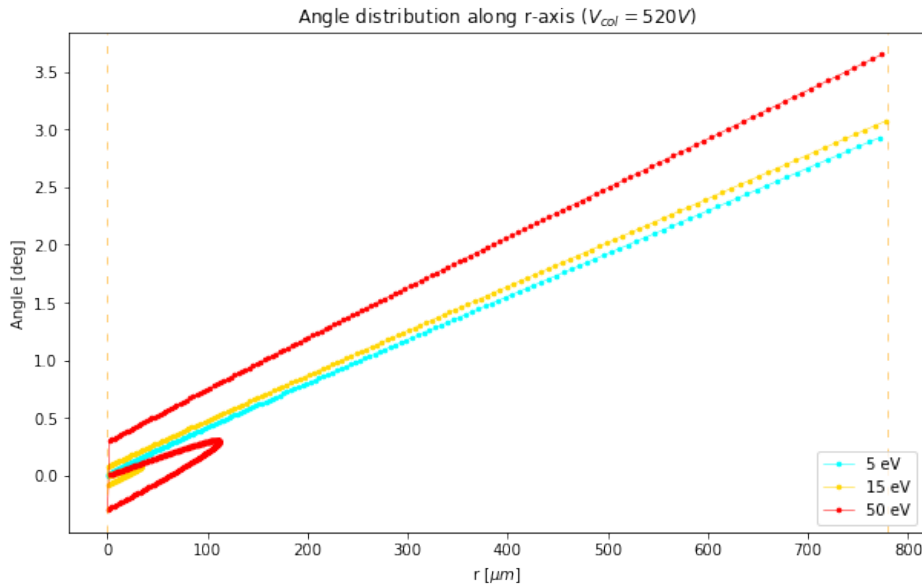


**Figure 3.9:** Angle distribution along the sample electrode as a function of position  $r$  on the sample electrode. All beams are collimated by  $V_{col} = 520$  V. Orange dashed lines indicate the limits of  $r$ . Note that different electrons with different trajectories can end up with the same position on the sample.

However, since there are millions of time steps involved in calculations and the kinetic energies of electrons rise up to  $\sim 3$  keV then drop down to several tens of eV within nanoseconds, calculation inaccuracies cannot be avoided.

There is another problem when plotting out the landing energies versus the angles of electrons. Figure 3.12 shows that there is some relation between the landing energies and angles, which should not happen since errors should be randomly distributed. If we plot out the trajectory of an electron with large energy error, we may find that it may have travelled too close to the electrodes (shown in Figure 3.12(b)) such that singularities may take place during calculation. Those electrons should have been absorbed by the electrode, yet due to finite mesh elements and time steps, they still land on the sample electrode. Generally for electrons that get too close to the electrodes, they may also have large angles. Hence the landing energy inaccuracies do relate to the angles in such way.

Yet, we have already found out that adding several tenths of eV to the landing energy does not influence the angle distribution significantly in the previous discussion. It is reasonable to agree that these calculation inaccuracies do not compromise the validity of the simulations so far.

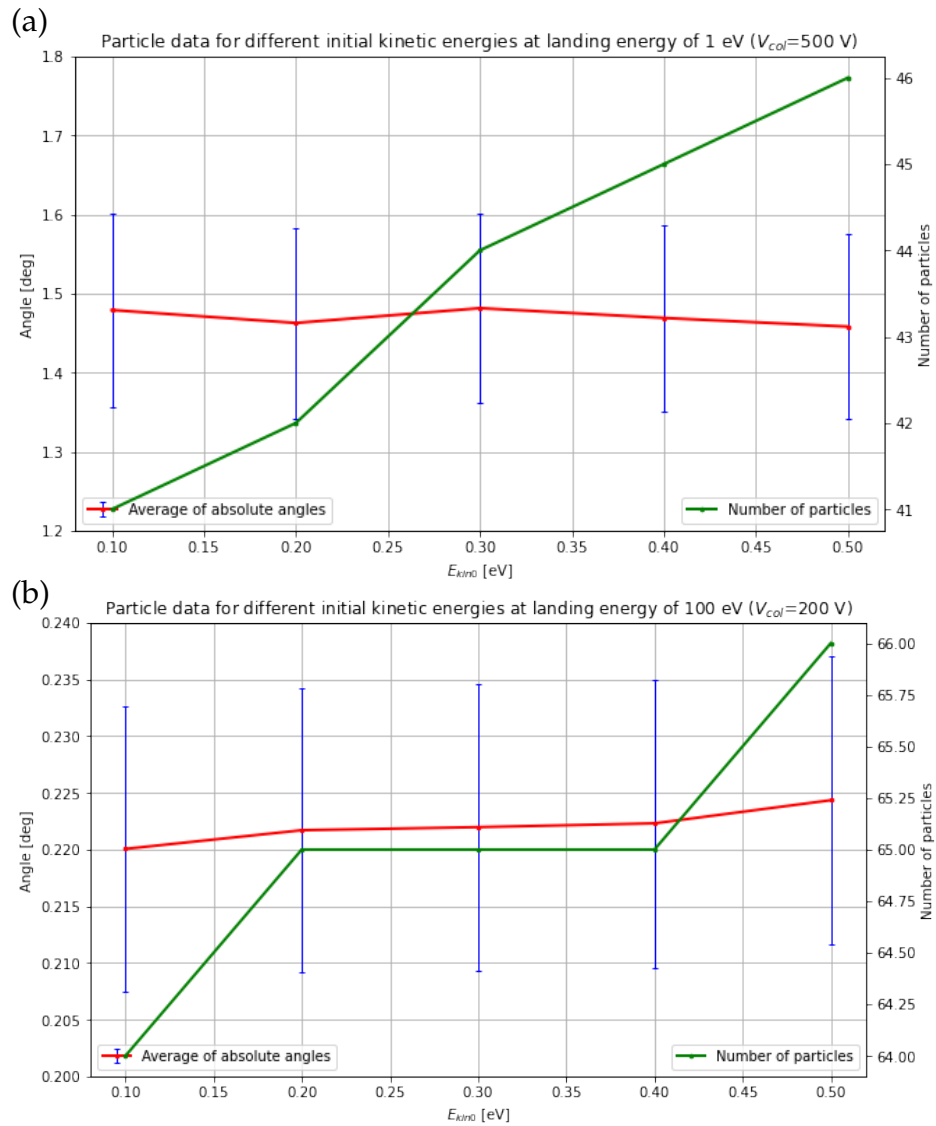


**Figure 3.10:** Electron data for different initial kinetic energies ( $E_{kin0}$ ) of 0.1 ~ 0.5 eV at landing energies of (a) 1 eV with  $V_{col} = 500$  V and (b) 100 eV with  $V_{col} = 200$  V. angle uncertainties are shown as blue error bars. Number of particles (out of 2000) are indicated as green lines.

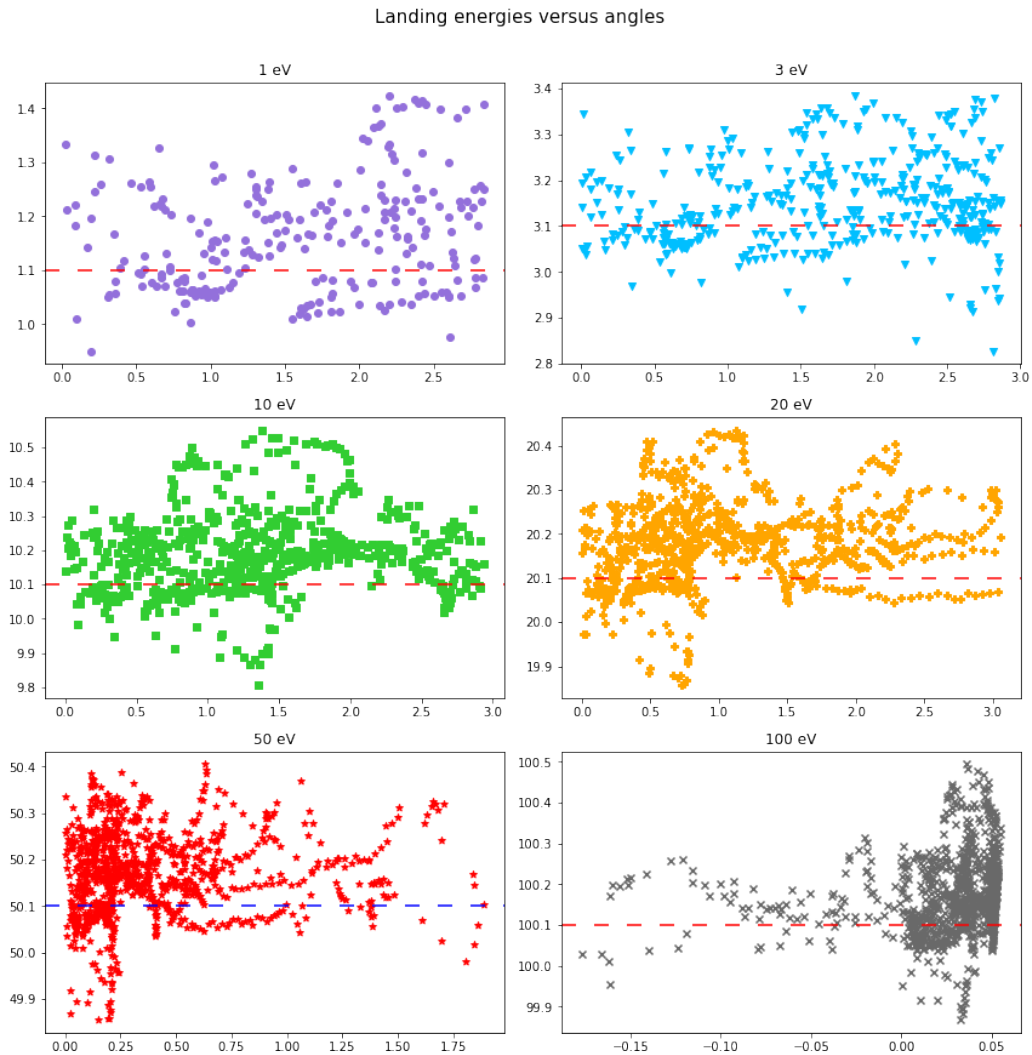


**Figure 3.11:** Scatter plot of landing energy with respect to the angles of electrons. The horizontal axes are angles and the vertical axes are landing energies. All beams are emitted with a total number of electrons of 1000 within an emission angle of  $1^\circ$  at a collimation voltage of 500 V. Dashed lines show the correct landing energy based on the law energy conservation.

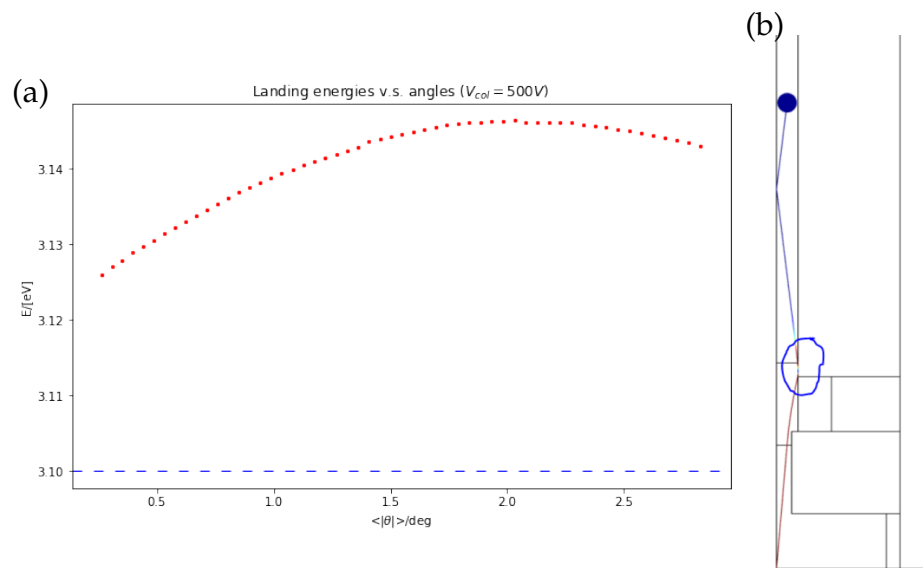


**Figure 3.12:** (a) Plot of Landing energies with respect to the angles of electrons, blue dashed line indicates the correct landing energy. The points seem not to distribute randomly since: 1) there are still too few electrons; 2) electrons with larger angles are more likely to have travelled closer to the electrode surfaces which can lead to larger calculation inaccuracies. (b) Electrons with large errors may have a travel history of getting too close the collimator (shown in the blue circle).

# Lensing Effect of the TEM-grid

## 4.1 Methods

As we are using both eV-TEM and LEEM in ESCHER, there will be a large field from LEEM electrostatic lenses. The lens tip (placed at M1 in Figure 2.8) and the sample form an electrostatic lens with a 15 kV voltage difference. Hence there will be an inhomogeneous electrostatic field towards the side of the eV-TEM gun of the grid (shown in Figure 4.1) and electrons that should hit the TEM-grid and disappear may be deflected and pass through holes that are not covered with a conductor and thus increase the intensity of current we will have in the end.

To analyse how this lensing effect would affect the current intensity, we will build up another simulation model to study the electric field around the TEM-grid first. Since our TEM-grid is only about 100 nm thick [17] and the whole geometry of the model is at a scale of several millimeters, this would cause a similar problem as we have already encountered in the eV-TEM simulation. Besides, calculating electric field and storing it may take few tens of gigabytes of memory, which is too large for the computer to handle. Hence the second step is to make the whole model smaller in size by cutting off the spaces where field is "homogeneous" or can be taken as "homogeneous" for a good approximation.

The TEM-grid we are using in the lab is a metal grid on a round silicon nitride support from PELCO<sup>®</sup>. It is 200 nm thick and has holes from 5  $\mu\text{m}$  down to 100 nm aligned in a hexagonal arrangement pattern. The window area is 0.5 mm  $\times$  0.5 mm, which is relatively small compared to the whole chip.

In our simulation, we set the window area same as the original size. Our grid holes have a radius of 1.25  $\mu\text{m}$  with a spacing of 5  $\mu\text{m}$  (shown

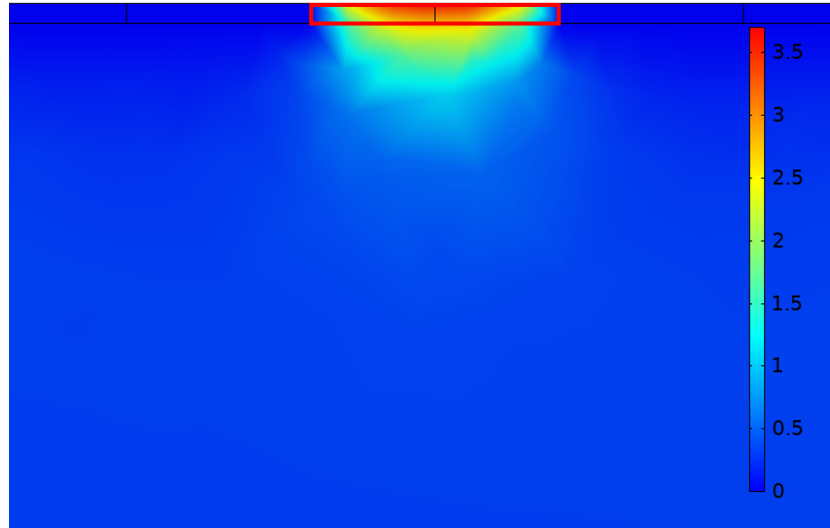


**Figure 4.1:** Potential “leakage” into the eV-TEM assembly below the TEM-grid. The red box labels the grid hole with a diameter of  $2.5\ \mu\text{m}$ .

in Figure 4.2). In the ESCHER configuration, the LEEM electrostatic lens M1 is  $1.5\ \text{mm}$  away from the TEM-grid, and there is a field-free drift space between the eV-TEM sample electrode and the TEM-grid. Hence we will set up a  $3\ \text{mm}$ -long block as the whole geometry.

But we will face the same issue as in the eV-TEM simulation where the TEM-grid is too thin compared to the whole geometry. Such a huge difference in length scale will cause trouble for mesh creation. Instead of looking into the whole model, we will be only interested to do the parts that have fields that contribute to lensing. When we make the geometry smaller, we can calculate that space with higher precision. Yet we can still use coarser meshes to estimate the equipotential surface near the TEM-grid and set up reasonable planes to make the model smaller. Figure 4.1 shows that the equipotential surfaces are not smooth enough as a result of coarse mesh and low resolution. We would also need to make fewer holes to simplify the model as much as possible. Ideally, the size of the final model will be at a scale of several micrometers.

## 4.2 Results and Discussions

Figure 4.3 shows the potential cut along the central line of the hole near the TEM-grid. Since the largest portion of the TEM-grid is still metal, it

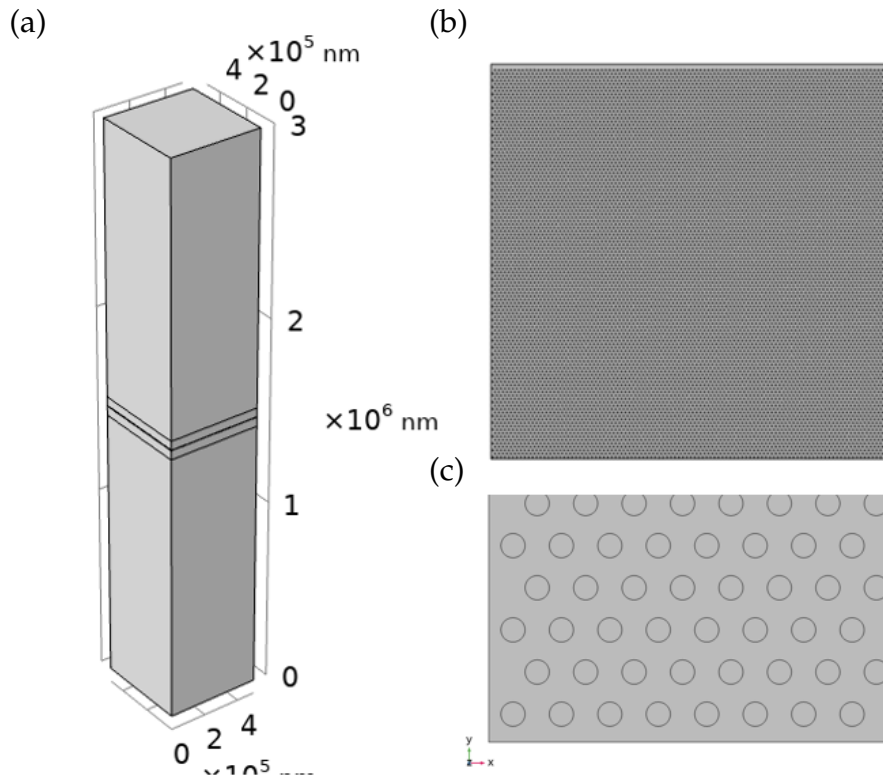


**Figure 4.2:** (a) Whole geometry of the TEM-grid simulation. The upper-most surface of the block has a fixed voltage of 15 kV. The lower half of the whole block surfaces is grounded. At the center of the block, there is another block for a finer mesh. At the center of the finer-mesh block lies the TEM-grid. (b) shows the TEM-grid hole arrays and (c) shows the zoomed-in left-lower corner of (b).

can still shield out most of the electrostatic field from the eV-TEM. Hence the potential below the TEM-grid should decay to 0 V rapidly, and the equipotential surface may be treated as flat in a good approximation. For the field above the TEM-grid, the overall electric field should look like that in between two parallel metal plates (see red dash line in Figure 4.3), where equipotential surfaces are parallel to the metal plates. Hence we can expect the equipotential surface to be flat enough somewhere above the TEM-grid.

From the boundary conditions of the electric field, it is obvious to find that the potential along the central lines of the holes should be the largest. Hence we should expect the equipotential surfaces to be flat when the potential is close to 0 V below the TEM-grid or close to the linear approxima-

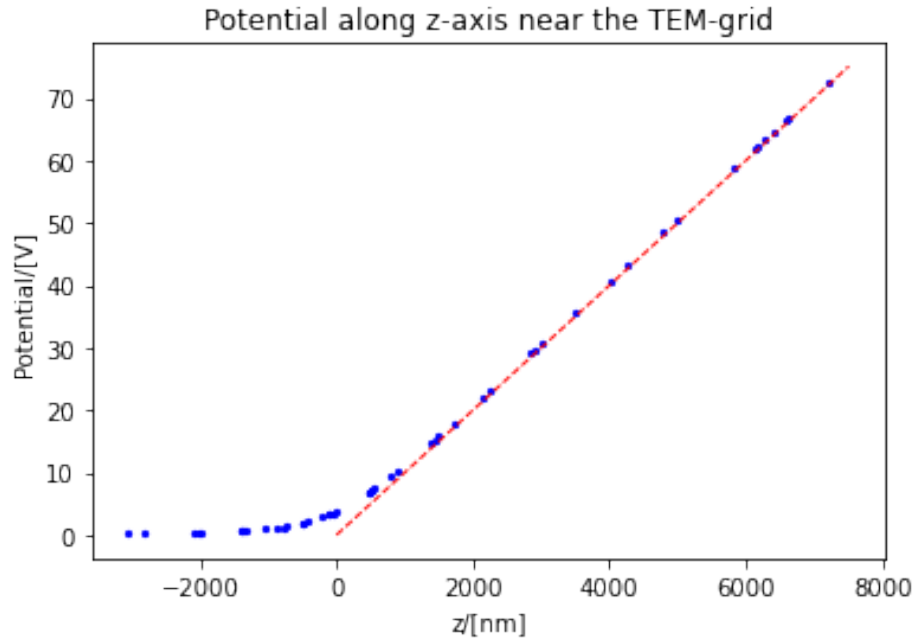


**Figure 4.3:** Potential near the TEM-grid. The center of the TEM-grid is located at  $z = 0$  nm. Blue dots indicates the potential values from the simulation and red dash line indicates the potential of two parallel metal plates.

tion line (indicated as red dashed line in Figure 4.3) above the TEM-grid. From Figure 4.3, we can see that the potential is close to 0 V after around  $2 \mu\text{m}$  below the TEM-grid. And the potential is close to the red dashed line after around  $2 \mu\text{m}$  above the TEM-grid. Hence the whole geometry can be  $\sim 10^3$  smaller than the real model in a good approximation.

In real experiments, there are mainly two hole arrangements of holes on the TEM-grids, namely hexagonal and square lattices. In our simulation, we would also like to reduce the size of our model into a small box with few holes on the TEM-grid. Hence we also studied the potential distribution in a single-hole TEM-grid model. Figure 4.4 shows that both hexagonal and square lattice TEM-grids show very similar potential distribution near the TEM-grids while that of single-hole TEM grid deviates from the other two TEM-grids after around  $1 \mu\text{m}$  below the TEM-grid. This can be understood by the density of holes on the TEM-grids. Suppose there are two holes far away from each other on an infinitely large TEM-grid, the potential down below the holes will decay fast since the size of the holes is small. If these two holes are moved closer together, the "leaked" potential through one hole will overlap with the other one, which leads to an increase of the potential. Hence as the density of holes

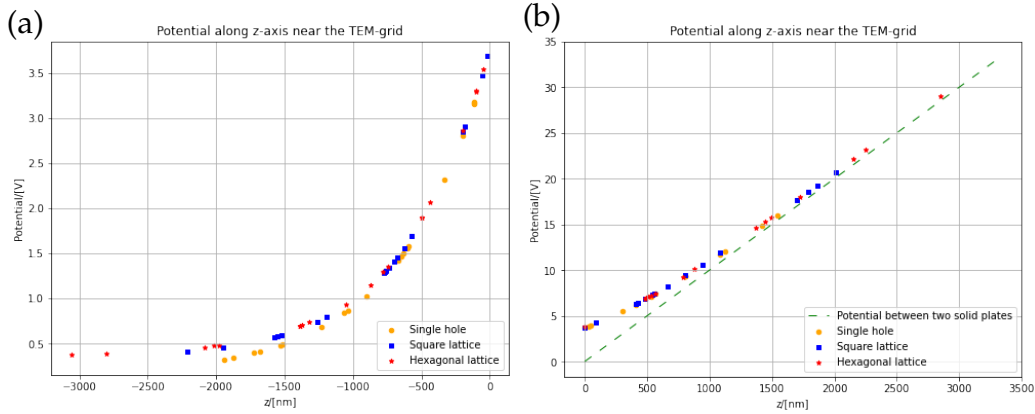


**Figure 4.4:** Potential distribution for three hole configurations along  $z$  axis (a) below and (b) above the TEM-grids. The TEM-grid locates at  $z = 0$  nm.

increases, there will be more overlapping and potential will decay slower. In both hexagonal and square lattices, the densities of holes do not differ much (shown in Figure 4.4), hence these two lattices can be substituted with each other despite negligible differences. However, applying periodic boundary conditions in the follow-up simulations may be much easier with square-lattice TEM-grid since it has less boundaries within a single unit cell than those in a hexagonal-lattice TEM-grid, hence we will use square-lattice TEM-grid for simulation.

Then it is important to determine reasonable cut-off equipotential planes for further simplification of the model in the vertical direction. Figure 4.5 shows the transverse potential distribution of the square-lattice TEM-grid. It is clear that the potential distribution is oscillating along the  $x$ -axis. And the wiggling pattern takes a *sine-wave* like feature when far away from the TEM-grid. The spacing between two maxima (minima) is  $5 \mu\text{m}$  since maxima appear at the center of the holes and the minima appear at the middle between two holes. As the distance increases, the amplitudes of the wiggling patterns decreases, which is in agreement with the theory. Since the amplitudes of the wiggling patterns at  $z = -3 \mu\text{m}$  and  $z = 2 \mu\text{m}$  are only around or even less than one-tenth of the average potential ( $V_0 \approx 0.307$  V at  $z = -3 \mu\text{m}$  and  $V \approx 20.507$  V at  $z = 2 \mu\text{m}$ ), the equipotential planes can be assumed to be flat at those heights. By cutting off the model along planes of  $z = -3 \mu\text{m}$  and  $z = 2 \mu\text{m}$ , the total size of the new model will be comparable to the size of the holes, which is now good for mesh creation.

In the square-lattice TEM-grid, the size of a single unit cell is two orders of magnitude smaller than that of the whole TEM-grid. Hence, the TEM-grid can be treated as infinitely large. To reduce the size of the model in

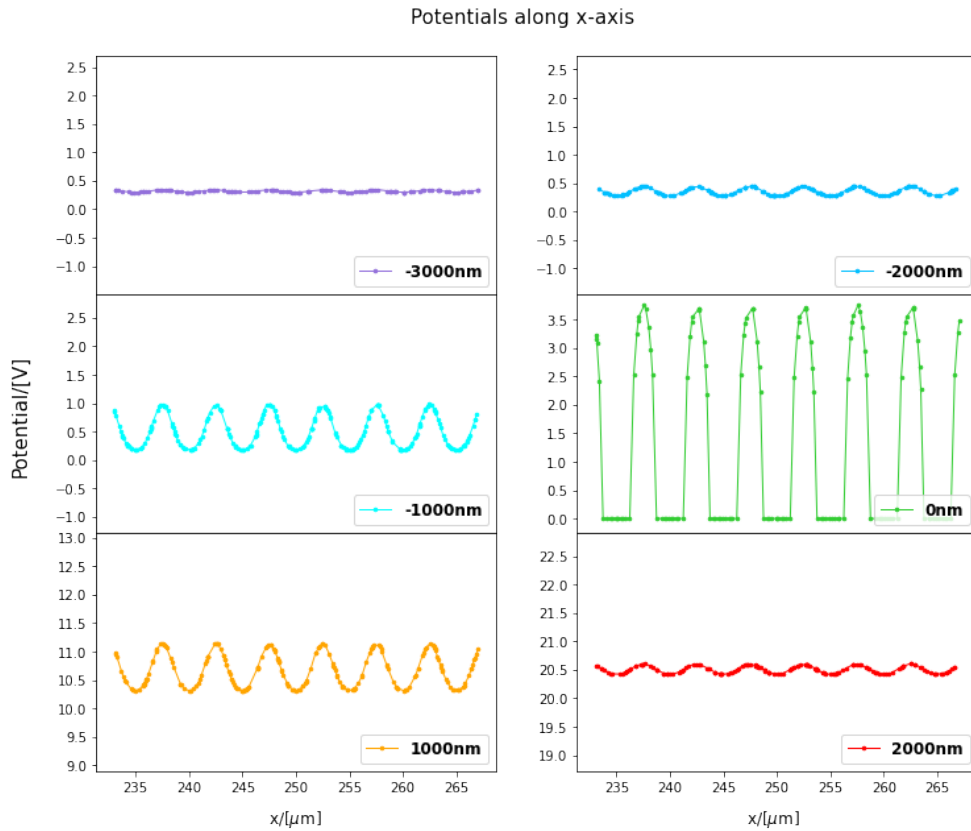


**Figure 4.5:** Transverse (along  $x$ -axis) potential distributions. All potential data is taken along lines which lie on the plane  $y = l_{tot}/2$  where  $l_{tot}$  is the width of the TEM-grid. The centers of holes also lie on that plane to show maxima and minima of potentials. Legends on the lower right corners of each subplots indicate the distance from the TEM-grid, and minus signs correspond to lines below the TEM-grid.

a more realistic way, we then applied periodic boundary conditions to the boundaries which unit cells share. By doing this, our model can then be physically equivalent to an infinitely large square-lattice TEM-grid. Figure 4.6 shows the potential distribution in the size-reduced model in comparison with the full-sized square lattice model. It is very promising that the potential in the size-reduced model is highly in agreement with the square lattice model in the previous discussion. And we can then send electrons from the flat surface below the TEM-grid in the size-reduced model.

In the particle tracing simulation, there is one more thing that we should take care of. Since the electrons come from the grounded sample electrode, electrons should have already gained energy after reaching at the cut-off

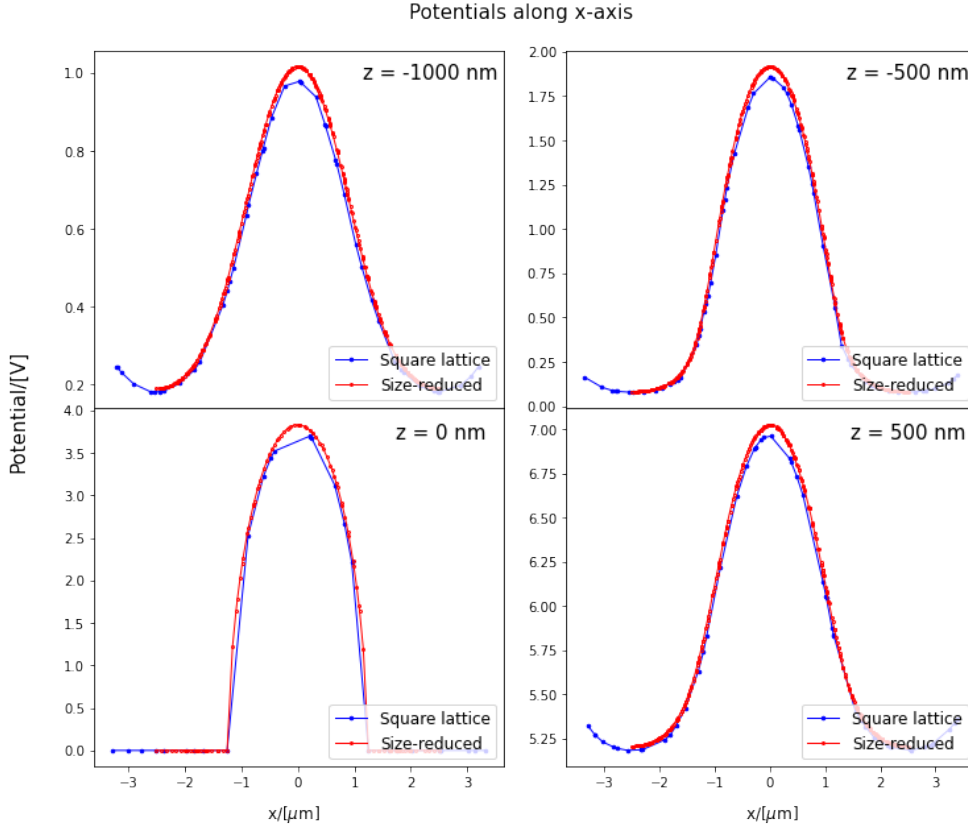


**Figure 4.6:** Transverse potential distribution in both square-lattice and size-reduced TEM-grid models at different heights.

equipotential surface due to potential difference between the cut-off plane and the sample electrode. Hence aside from the landing energy which is determined by the eV-TEM gun, we should also add an extra kinetic energy of  $E_{kin}^{ext} = e \times V_0 \approx 0.307$  eV. Since equipotential surfaces can be approximated to be parallel below the lower cut-off plane, electrons can barely feel the forces in the transverse plane, therefore we can still set the initial velocity of the electrons to be perpendicular to the lower cut-off plane in the size-reduced model.

Figure 4.7 shows the lensing effect of two typical landing energies of 1 and 100 eV. The lensing effect in Figure 4.7 (a) is very obvious as the parallel beams form into a cone above the TEM-grid. The lensing effect in Figure 4.7(b) however is not very obvious. This is because the energy gain by the leaked voltage is around 3 eV, which is comparable to  $E_{kin0} = 1$  eV yet negligible to  $E_{kin0} = 100$  eV. In our simulations, we set 2500 electrons in total with equal spacing. Table 4.1 shows the electron counts in different

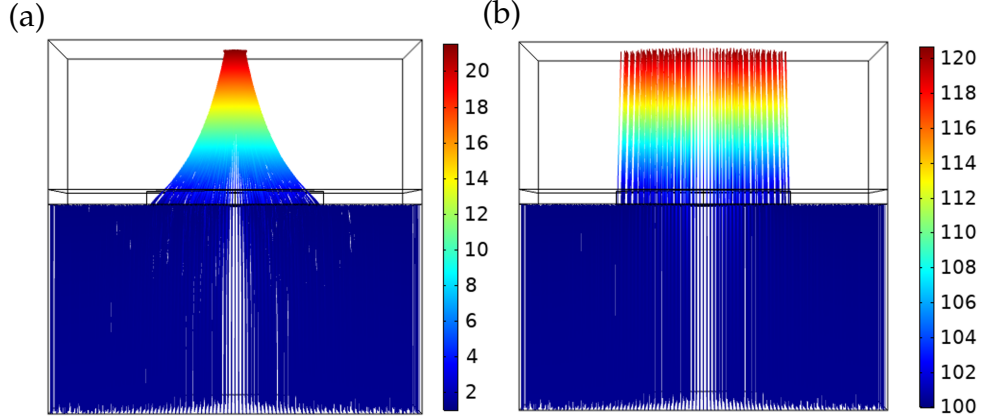


**Figure 4.7:** Electron trajectories with landing energy of (a) 1 eV and (b) 100 eV. Color bars indicate the kinetic energies of electrons.

cases. The theoretical count without lensing effect is calculated by:

$$N = \frac{\pi r_{hole}^2}{l_{cell}^2} \cdot 2500 = \frac{\pi \cdot (1.25 \mu\text{m})^2}{(5 \mu\text{m})^2} \approx 491 \quad (4.1)$$

where  $r_{hole}$  is the radius of the hole and  $l_{cell}$  is the length of the unit cell, which is in agreement with the simulation result when no lensing effect happens.

In Table 4.1, the current intensity increases by over 40% at landing energy of 1 eV, whereas nearly no current increase takes place for landing energy of 100 eV. Hence, the lensing effect will be less and less noticeable as the landing energy of the electrons increases as a result of comparable extra energy gain due to leaked voltage. Therefore, we should be careful with the lensing effect when using low energy electrons, especially close to mirror mode.

Electron energy	1 eV	5 eV	10 eV	50 eV	100 eV	No lensing ( $I_0$ )
Counts	700	530	520	485	485	484
Relative intensity $I/I_0$	1.446	1.095	1.074	1.002	1.002	1

**Table 4.1:** Electron counts

Since the images are converged from k-space by Fourier transformation, it is helpful for us to trace back the electrons that are affected by the lensing effect by looking at their k-vectors. Figure 4.8 shows the histograms of in-plane k-vectors. By studying the distribution of the in-plane k-vectors, we can then numerically calibrate the electron flux incident on the camera in ESCHER.

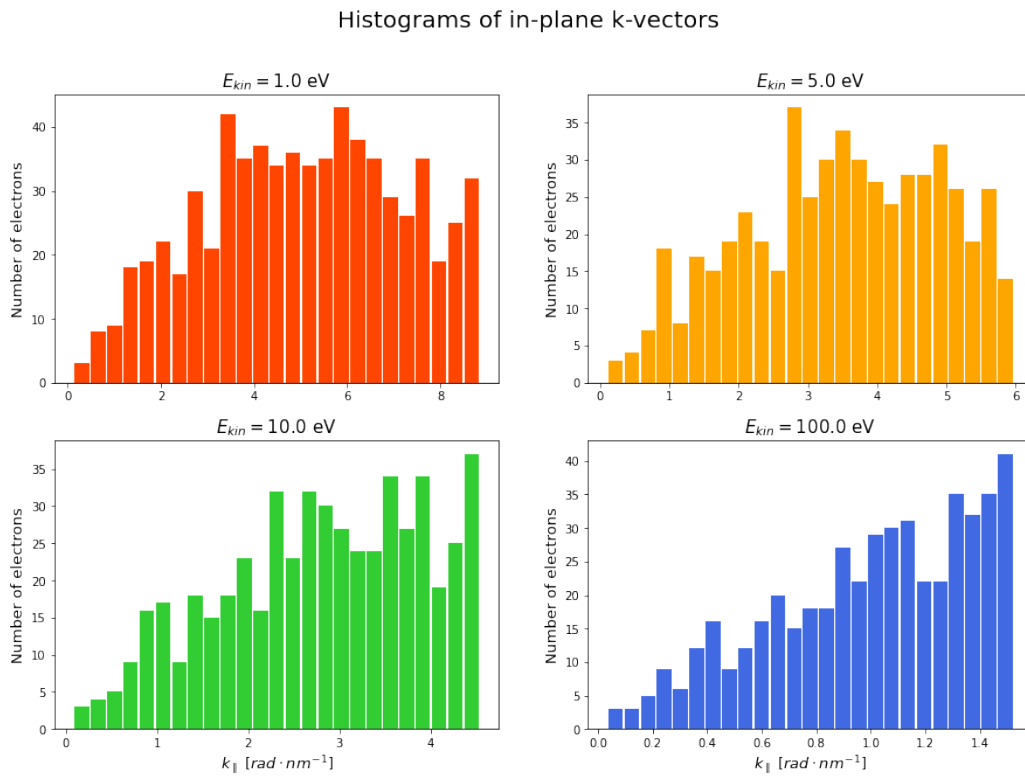


**Figure 4.8:** Histograms of in-plane k-vectors ( $k_{||}$ ) for different landing energies. Notice that the horizontal axes vary from around 1.5 rad/nm to 9 rad/nm. The limit of  $k_{||}$ -axis is decreasing as the landing energy increases, which can also prove that the lensing effect is less and less obvious as the landing energy increases.



## Conclusion

In previous chapters, we have introduced the need for an eV-TEM with a new design. We have set up models to run simulations in COMSOL to test if the new design works. In eV-TEM simulations, the collimation voltage is playing a major part in collimating the electron beams. For various landing energies, the collimation voltage which gives the best collimation is gradually increasing as the landing energy increases. The current density also increases with the landing energy. At  $V_{col} \simeq 520$  V, the current density reaches maximum while giving the lowest angle distribution. Hence we would recommend to collimate electron beams with collimation voltage around 520 V. It is also noticeable that the best collimation voltage does not change much as the landing energy increases. This also implies that the influence from the second electrostatic lens formed by the field between sample and collimator is rather negligible. If we were to have a fourth electrode in between the sample and collimator, this can enable best collimation from the collimator and also fine-tune the collimation before the sample electrode. However, there are only 3 voltage input connections available in ESCHER, further re-design may be needed for this fine-tune feature.

We have also studied that the eV-TEM with field emission tip can give very small angle distribution with an average of absolute angle less than  $1^\circ$ . And better angle spread further proves that using a field emitter is feasible, which has an inherently smaller energy distribution. We also sent electrons with different initial kinetic energies  $E_{kin0}$  to simulate the energy distribution caused by field emission. The results show that the influence on angle distribution brought by initial kinetic energies  $E_{kin0}$  is rather negligible. This initial kinetic energy distribution simulation also proves that our simulations remain valid despite noticeable energy errors due to cal-

ulation inaccuracies.

In the simulations of TEM-grid, we successfully reduced the size of the whole model. We also applied periodic boundary conditions to simulate infinitely large square-lattice TEM-grid, the result of which shows high agreement with the TEM-grid simulation in real size. Then we studied the lensing effect based on the size-reduced model. The lensing effect becomes more and more negligible as the landing energy of electrons decreases, which could be problematic for aberration correction. This way we can calibrate the electron flux incident on the camera in ESCHER.

Now we are confident that building the simulated eV-TEM gun will improve the energy spread to the same as in LEEM mode, which enables better spectroscopy. Also this design, with the long drift tube, allows for adding tunable deflectors, which can improve position and incidence angle of the beam on the sample, if the sample is not mounted straight or the relevant areas are on the edge of the TEM-grid.

## Acknowledgement

I started this research as my first Master project from July, 2021. I was fascinated by the handy tool named COMSOL, even though it was not very cooperative from time to time. In the meantime, I was warmly welcomed by the group members. They were like family to me through the hard times during the pandemic of COVID-19. I am very grateful to have Prof. Sense Jan van der Molen as my supervisor, who is always willing to offer help when I need it most. My daily supervisor, Peter Neu, is like an older brother to me. He assisted me with various academic problems and gave very practical solutions all the time. It is very generous that Norman offered his lab computer for my simulations, without which none of my simulations could be done. Coffee breaks with Leander Kalff are very refreshing as we can always exchange the ideas of our own projects. He also shared lots of literature and data for me to finish this thesis, which is very helpful to make my thesis more comprehensible. It is also a pleasure to have Tristan Havinga as my office pal. He is always a good listener and helped me a lot with various languages especially English and Dutch. I really enjoy the Asian snacks from him, so I also brought many snacks of my favorite for sharing, which in the end turned into an idea to set up a snack bar in our office open to everyone who needs a candy during break. Even though I usually had lunches along, I still quite enjoy lunch time with Thomas Oosterholt, Mio Poortvliet, Leader as well as Tristan. It was fun talking about everything in every topic and exchanging different ideas. I would also thank Tobias, Amin, Arash and Xing for their help during or outside the group meetings. Especially, Tobias is always very enthusiastic and genius on scientific or nonscientific jokes, which saved me from sleepiness since I find getting up at 7 is very hard for me. At the beginning of my project, I also received lots of assistance from the ICT group,

of which I am very thankful. Finally, I would like to thank my parents for supporting my master study at Leiden. Even though I have to be honest with the fact that I do not really enjoy chatter and pressure from them, I'm still always grateful that they give me everything they have to encourage me to see the awe of the world. You are the best parents I've ever known in this world!

# Bibliography

- [1] D. Geelen, J. Jobst, E. E. Krasovskii, S. J. van der Molen, and R. M. Tromp. Nonuniversal transverse electron mean free path through few-layer graphene. Phys. Rev. Lett., 123:086802, Aug 2019.
- [2] R.M. Tromp, J.B. Hannon, A.W. Ellis, W. Wan, A. Berghaus, and O. Schaff. A new aberration-corrected, energy-filtered leem/peem instrument. i. principles and design. Ultramicroscopy, 110(7):852–861, 2010.
- [3] Rolf Erni, Marta D. Rossell, Christian Kisielowski, and Ulrich Dahmen. Atomic-resolution imaging with a sub-50-pm electron probe. Phys. Rev. Lett., 102:096101, Mar 2009.
- [4] P. E. Batson, N. Dellby, and O. L. Krivanek. Sub-ångstrom resolution using aberration corrected electron optics. Nature, 418(6898):617–620, Aug 2002.
- [5] Daniël Geelen, Aniket Thete, Oliver Schaff, Alexander Kaiser, Sense Jan van der Molen, and Rudolf Tromp. ev-tem: Transmission electron microscopy in a low energy cathode lens instrument. Ultramicroscopy, 159:482–487, 2015. Special Issue: LEEM-PEEM 9.
- [6] Peter S. Neu, Daniël Geelen, Aniket Thete, Rudolf M. Tromp, and Sense Jan van der Molen. Complementary leem and ev-tem for imaging and spectroscopy. Ultramicroscopy, 222:113199, 2021.
- [7] S. M. Schramm, J. Kautz, A. Berghaus, O. Schaff, R. M. Tromp, and S. J. van der Molen. Low-energy electron microscopy and spectroscopy with escher: Status and prospects. IBM Journal of Research and Development, 55(4):1:1–1:7, 2011.

- 
- [8] N. P. Carleton. Electrostatic lens. Review of Scientific Instruments, 28(1):9–10, 1957.
- [9] T. Kogure. Chapter 2.9 - electron microscopy. In Faïza Bergaya and Gerhard Lagaly, editors, Handbook of Clay Science, volume 5 of Developments in Clay Science, pages 275–317. Elsevier, 2013.
- [10] Elprocus. What is fermi dirac distribution? energy band diagram, and boltzmann approximation. <https://www.elprocus.com/fermi-dirac-distribution-energy-band-diagram-and-boltzmann-approximation/>.
- [11] Patterson and Alex Andrew. Theory and modeling of field electron emission from low-dimensional electron systems. pages 253–271, 2018.
- [12] J. J. Saenz, N. Garcia, Thien Binh Vu, and H. De Raedt. Field Electron Emission from Atomic-Size Microtips, pages 409–441. Springer Netherlands, Dordrecht, 1990.
- [13] M Knoll and E Ruska. Das elektronenmikroskop. Zeitschrift für Physik, 78(5):318–339, May 1932.
- [14] Miroslav Karlík. Lattice imaging in transmission electron microscopy. 2001.
- [15] Linda E. Franken, Kay GrÄnewald, Egbert J. Boekema, and Marc C. A. Stuart. A technical introduction to transmission electron microscopy for soft-matter: Imaging, possibilities, choices, and technical developments. Small, 16(14):1906198, 2020.
- [16] M. P. Seah and W. A. Dench. Quantitative electron spectroscopy of surfaces: A standard data base for electron inelastic mean free paths in solids. Surface and Interface Analysis, 1(1):2–11, 1979.
- [17] Pelco holey silicon nitride support film for tem. <https://www.tedpella.com/grids.html/silicon-nitride-holely.aspx>.